OPEN ACCESS



Early Planet Formation in Embedded Disks (eDisk). IV. The Ringed and Warped Structure of the Disk around the Class I Protostar L1489 IRS

Yoshihide Yamatoo, Yuri Aikawa o, Nagayoshi Ohasho, John J. Tobino, Jes K. Jørgenséo, Shigehisa Takakuwao, Yusuke Ason, Jinshi Sai (Insa Chor), Christian Flores, Itziar de Gregorio-Monsalvo, Shingo Hirando, Ilseung Haĥ⁸, Miyu Kido⁵, Patrick M. Koch², Woojin Kwon^{9,10}, Shih-Ping Lar^{2,11,12,13}, Chang Won Lee⁸ Jeong-Eun Lee D., Zhi-Yun Li 50, Zhe-Yu Daniel Lin Leslie W. Looney 60, Shoji Mori 70, Suchitra Narayana No. Nguyen Thi Phuong 190, Kazuya Saigo, Alejandro Santamaría-Mirando, Rajeeb Sharm, Travis J. Thieme 1,12,130, Kengo Tomida 70, Merel L. R. van 't Hoff 200, and Hsi-Wei Yer 0 ¹ Department of AstronomyGraduate School of Scienc**∉**he University of Tokyo,7-3-1 Hongo,Bunkyo-ku,Tokyo 113-0033,Japan ² Academia Sinica Institute of Astronomy & Astrophysics, 11F of Astronomy-Mathematics Building, AS/NTU, No. 1, Sec. 4, Roosevelt Rd, Taipei 10617, Taiwan, R.O.C. ³ National Radio Astronomy Observator §20 Edgemont Rd. Charlottesville, VA 22903, USA Asitorial Radio Astronomy Observators and Engineering, VA 22003, Copenhagen KDenmark

Niels Bohr Institute, University of Copenhagen Øster Voldgade 5-7DK-1350, Copenhagen KDenmark

Department of Physics and Astronomy, Graduate School of Science and Engineering, Kagoshima University, 1-21-35 Korimoto, Kagoshima, Kagoshima 890-006 Japan ⁶ Korea Aştronomy and Space Science Instit**ut∉**β Daedeok-daer**ல்**useong-guDaejeon 34055Republic of Korea European Southern Observato Alonso de Cordova 3107 Casilla 19, Vitacura, Santiago Chile ⁸ Division of Astronomy and Space Science niversity of Science and Technolog2.17 Gajeong-roYuseong-guDaejeon 34113Republic of Korea Department of Earth Science Education National University Gwanak-ro, Gwanak-gu, Seoul 08826 Republic of Korea SNU Astronomy Research Cent⊛eoul National University1 Gwanak-ro,Gwanak-gu,Seoul 08826Republic of Korea Institute of Astronomy, National Tsing Hua University No. 101, Section 2, Kuang-Fu Rd, Hsinchu 30013, Taiwan Center for Informatics and Computation in Astronom**N**ational Tsing Hua UniversityNo. 101, Section 2,Kuang-Fu Rd,Hsinchu 30013,Taiwan

13 Department of PhysicsNational Tsing Hua UniversityNo. 101, Section 2,Kuang-Fu Rd,Hsinchu 30013,Taiwan 14 Department of Physics and Astronom\(\)eoul National University1 Gwanak-ro,Gwanak-gu,Seoul 08826\(\)Republic of Korea \(\)
15 University of Virginia, 530 McCormick Rd.,Charlottesville,Virginia 22904,USA ¹⁶Department of AstronomyUniversity of Illinois, 1002 West Green StUrbana,IL 61801, USA ¹⁷ Astronomical InstituteGraduate School of Sciencephoku University,Sendai 980-857&Japan ¹⁸ Institute for Astronomy,University of Hawai'i at Mānoa,2680 Woodlawn Dr.,Honolulu, HI 96822, USA Department of Astrophysics, Vietnam National Space Center, Vietnam Academy of Science and Techonology, 18 Hoang Quoc Viet, Cau Giay, Hanoi, Vietnam Operation of Astronomy University of Michigan, 1085 S.University Ave., Ann Arbor, MI 48109-1107, USA Received 2023 January 24; revised 2023 March 25; accepted 2023 April 14; published 2023 June 28

Abstract

Constraining the physical and chemical structure of young embedded disks is crucial for understanding the earliest stages of planet formation. As part of the Early Planet Formation in Embedded Disks Atacama Large Millimeter/ submillimeterArray Large Program,we presenthigh spatial resolution (~0."1 or ~15 au) observations of the 1.3 mm continuum and CO J = 2-1, C O J = 2-1, and SO $_{\rm N}$ = 6_5 - 5_4 molecular lines toward the disk around the Class I protostar L1489 IRS he continuum emission shows a ring-like structure 56 au from the central protostar and tenuous, optically thin emission extending beyond ~300 al3COnemission traces the warm disk surface, while the CO emission originates from near the disk midplane. The coincidence of the radial emission peak of C¹⁸O with the dust ring may indicate a gap-ring structure in the gaseous disk as Weel.SO emission shows a highly complex distributionincluding a compact prominent component at □30 auwhich is likely to originate from thermally sublimated SO molecules. The compact SO emission also shows a velocity gradient along a direction tilted slightly (~15°) with respect to the major axis of the dustlisk, which we interpretas an inner warped disk in addition to the warp around ~200 au suggested by previous work. These warped structures may be formed by a planet or companion with an inclined orbitr by a gradual change in the angular momentum axis during gas infall.

Unified Astronomy Thesaurus concepts: Protoplanetary disks (1300); Protostars (1302); Planetary system formation (1257)

1. Introduction

Circumstellar disks are the birthplaces of planets. Constrain processes planetary system formation. The physical and chemical structure of Class II disks has been studied in great

Original content from this work may be used under the terms of the Creative Commons Attribution 4.0 licence. Any further distribution of this work must maintain attribution to the author(s) and the title of the work, journal citation and DOI.

with the Atacama Large Millimeter/submillimeter Array (ALMA) (e.g., Andrews et al. 2018; Öberg et al. 2021). These ing the structure of disks is thus essential for understanding the studies have revealed that substructures such as rings and gaps are present in both dust and gas, suggesting that planet formation is ongoing in Class II disks. Furthermore, the detail through dust continuum and molecular line observations presence of formed planets has recently become more apparent through the detection of velocity kinks in channel maps of bright molecular line emission (e.g., Pinte et al. 2018b; Teague et al. 2019), in addition to direct detections of circumplanetary disks within gaps (e.g., Keppler et al. 2018; Benisty et al. 2021; Bae et al.2022).

suggests that planet formation could have started in the earlier between the inner and outer disks (Sai et al. 2020). Dust evolutionary stages. It is thus essential to study what is happening in disks around younger Class 0/I protostarsin order to obtain a complete picture of planet formation processes Recent ALMA observations have revealed substructures in dust continuum emission in a handful of Class 0/I northeast-southwestlirection. Furthermore, Ohashi et al. disks (e.g., ALMA Partnership et al. 2015; Sheehan & Eisner 2018: Segura-Cox et al. 2020: Sheehan et al. 2020). suggesting that the first steps toward planet formation may be dust growth,or even planet formation. ocurring while these young disks are stillembedded in their natal envelopes. Grain growth has also been suggested in embedded young disks (e.g., Harsono et al. 2018). In addition, embedded disk around L1489 IRS as part of the eDisk ALMA recentsurveys have shown that mass of Class II disks is insufficient for giant planets to be formed, while Class 0/I disks describe the observational details in Section 2 and the are massive enough (e.g. ychoniec et al. 2021).

Motivated by these previous studies, the Early Planet Formation in Embedded Disks (eDisk) ALMA Large Program (Ohashi et al. 2023) was initiated with the main goal of understanding how early substructures form in the disks arounfinally summarized in Section 6. young protostars. The core of eDisk is a high-resolution systematic survey of the dust continuum substructures down to ~5 au scales in 19 young embedded sources. In addition to the dust continuum, several molecular lines, mainly CO isotopolog lines, have been observed to probe the gas distributions and kinematics in the embedded disks as well as in the envelopes. Directors Discretionary Time (DDT)program (projectcode:

One of the sources of the eDisk sample is the Class I protostarL1489 IRS (or IRAS 04016+2610), located in the Taurus molecular cloudWhile severalrecentstudies assume ~140 pc as the distance to L1489 IRS (e.gMercimek et al. 2022; Sai et al. 2022) based on the average distance over the Taurus region (141 ± 7 pcZucker et al. 2019), Roccatagliata et al. (2020) estimate the distancesto six different stellar population groups in the Taurus region using Gaia measurements. One of the groups (Taurus F in the original paper) with urations were conducted in 2021 August, while the three an estimated distance of 146 pc includes a nearby source to L1489 IRS (with a separation of 12¢). Thus, in the present work, we assume thathe distance to L1489 IRS is 146 pc When this distance as well as the updated photometry from near-infrared to millimeter wavelengths is taken into account, the bolometric luminosity and bolometric temperatureare 3.4 Le and 213 K, respectively (Ohashiet al. 2023), from which L1489 IRS is classified as a Class I source.

L1489 IRS is embeddedin a ~2000au scale infallingrotating envelope, as revealed by single-dish observations (Hogerheijde & Sandell 2000; Motte & André 2001). A bipolar outflow along the northwest-southeastlirection is also identified by infrared and submillimeter line observations (Tamura et al. 1991; Hogerheijde et al. 1998). Brinch et al. (2007) first detected a rotation signature at ~200–300 au scale using ~1" resolution HCO+ line observations with the Submillimeter Array (SMA), which was interpreted as a Keplerian disk. ALMA observations of the ¹²CO and C¹⁸O a radius of ~600-700 au and a centratellar mass of 1.6 M (Yen et al. 2014). Yen et al. (2014) also detected a streamerlike infalling flow feeding the material to the central protostellar disk with the $C^{18}O$ J = 2–1 emission. Higherresolution (~0 3) C¹⁸O line observations with ALMA

The presence of substructures and planets in Class II disks revealed that he disk is warped at the boundary (r ~ 200 au) continuum images obtained with ALMA (Yen et al. 2014; Sai et al. 2020) and the Combined Array for Researchin Millimeter-wave Astronomy (CARMA: Sheehan & Eisner 2017) also show a disk-like structure elongated along the (2022a) tentatively detect ring-like structure atr ~ 90 au in the 1.3 mm dust continuum emission which may be a hint of

In this paper, we present high spatial resolution (~0."1) observations of dust continuum and molecular lines toward the Large Program. This paper is structured as follows. We observational results (image maps and radial profiles) in Section 3. Section 4 presents the analysis of the dust continuum and CO isotopolog line data to constrain the physical structures of the disk. The results are discussed in Section 5 and are

2. Observations and Data Reduction

L1489 IRS was observed as part of the eDisk Large Program (project code: 2019.1.00261.L, PI: N. Ohashi) and a dedicated 2019.A.00034.SPI: J. J. Tobin). Details of the observations and data reduction procedures are provided in Ohasbt al. (2023). Here we summarize the key aspects specific to L1489 IRS. Our observationswere made in a total of five executions, two of which used extended antenna configurations (C43-8) from the Large Program, and the other three used compact antenna configurations (C43-5) from the DDT program. The two executions with extended antenna configexecutions with compactantenna configurations in the DDT program were conducted in 2021 December and 2022 July.

The eDisk program is designed to observe the dust continuum at 1.3 mm (or 225 GHz), as well as several molecular lines. The targeted molecular lines are listed in Table 2 of Ohashi et al. (2023). In this specific first-look paper on L1489 IRS, we focused on three molecular lines: 13CO J = 2-1, $C^{18}O J = 2-1$, and $SO_{N} = 6.5-54$. In addition to these lines, several other lines 2CO, DCN, H2CO, and c-GH2) are also detected, while SiO and QDH lines are not detected (see Table 2 in Ohashi et al. 2023, for the complete list of the targeted transitions).

The initial calibration was performed by the ALMA observatory using the standard ALMA calibration pipeline version 2021.2.0.128. We then carried out self-calibration using Common Astronomy Software Applications (CASA) version 6.2.1 (McMullin et al.2007). Prior to self-calibration, we imaged the continuum data of each execution block (J = 2–1) lines confirmed the presence of a Keplerian disk with separately. We then found an emission peak on each image and aligned the peaks to a common phase center using the CASA task fixvis and fixplanets. For the aligned visibilities we applied an amplitude rescaling by inspecting the azimuthally averaged visibilities (amplitude profile against baseline length) from different executions to corrector possible flux calibration uncertainties (see Ohashi et 2023).

> We then performed four iterations of phase-only selfcalibration and then two iterations of phase and amplitude self-calibration on the compactonfiguration continuum data.

²¹ We note that there is an independent stimate of the distance toward the neighboring molecular cloud L1498 of 129 pc (Zucker et. 2020), which is significantly different from the 146 pc adopted here.

Table 1 Properties of the Continuum and Line Images

	Frequency (GHz)	E _{up} a,b (K)	Spectral Resolution (km s ⁻¹)	Channel Width (km s ⁻¹)	Robust	Beam Size (PA)	rms (mJy beam̄¹)
continuum	225	L	L	L	1.0	0."105 × 0 Ø78 (12°)	0.014
continuum (tapered)	225	L	L	L	2.0	0.1221 × 0.1179 (11°)	0.018
¹³ CO J = 2–1	220.398684 <mark>2</mark>	15.9	0.17	0.20	1.0	0."13 × 0 .11 (8.9°)	2.4
$C^{18}O J = 2-1$	219.560354 <mark>1</mark>	15.8	0.17	0.20	1.0	0!/13 × 0 /10 (13°)	1.7
SO $J_N = 6_5 - 5_4$	219.949442 <mark>0</mark>	35	0.17	0.20	1.0	0."13 × 0 .10 (15°)	2.1

data and were self-calibrated together the combined data. we performed two iterations of phase-only self-calibration and no phase+amplitude self-calibration. The self-calibration solutions were then applied to the line data-inally, the line data were continuum subtracted using the CASA task uvcontsub in the visibility domain.

For the continuum datawe CLEANed down to two times the rms noise level using different Briggs robust parameters, asve mainly focus on the morphology of the emissione, adopt shown in Appendix A. The auto-multithresh algorithm implemented in CASA was used to generate the CLEAN masks. We adopted the image with robust =1.0 as representative image considering the balance between spatial exception is Section 4.1, where we compare the flux density resolution and sensitivity. The resulting beam size and rms noise level of the continuum image are 0 105 × 0 078 (PA =12°) and 14 µJy beam, respectively (Table 1). We note that the beam size of the representative image is a factoof ≈2 larger than the typical spatial resolution of other eDisk continuum images (≈0 05); because the continuum emission of the L1489 IRS disk is faint, we need to trade off spatial resolution for better sensitivityAdditionally, to clearly show the extended, faint emission, we made another continuum image with robust =2.0 and uvtaper =1000 k λ . has a beam size and rms noise lever 0'221 × 0'179 (PA =11°) and 18 µJy beam, respectively (Table 1). For the line data, we CLEANed down to three times the rms noise level with robust = 1.0 (and uvtaper = 2000 k λ as the default imaging parameterof eDisk line images; see Ohashiet al. 2023) for all lines presented in this paperAs in the case of continuum imaging, the auto-multithresh algorithm implemented in CASA was used to generate the CLEAN masks. The typical beam size and rms noise level f the line images are 0 1 and 2 mJy beamat a velocity channel width of 0.2 km s⁻¹, respectively. We assume an absolute flux calibration uncertainty of 10%. The maximum recoverable scale is ~2 4. 22 The detailed properties of the continuum image and line image cubes, as well as the corresponding spectroscopic data reported in Table 43

van Moorsel 1995; Czekala etal. 2021): the inconsistency of intensity units between the CLEANed modelmage and the residualimage makes the intensity in the resulting CLEANed image incorrect(see Figure 3 in Czekala et al. 2021 for a

The data were then combined with the extended configuration comprehensive illustration call (2021) introduced a method to correctfor this effect (JvM correction). However, while the JvM correction recovers the correct intensity scales in the restored imagescorrecting the data in this way artificially manipulates the noise level by rescaling the residual image and may exaggerate the signal-to-noise ratio (S/N)Casassu& Cárcamo 2022). The modification of the S/N could lead to the misinterpretation of the structure and extent of emissionce the images without JvM correction. We only use the JvMcorrected image when we estimate the donates based on the flux density of the continuum emission in Section 3.1. Another estimated from the visibility analysis with that measured on the image plane because the visibility analysis is not affected by the JvM effect.

Observational Result

3.1. 1.3 mm Continuum

Figure 1 shows the 1.3 mm dustontinuum images of the L1489 IRS disk. The left panel of Figure 1 shows the largescale view of the continuum emission with robust = 2.0 and uvtaper = 1000 kλ, while the middle and right panels show the zoom-in view with robust = 1.0. A disk-like structure elongated along the northeasto the southwest direction is detected, which is consistent with previous observations (Yen et al. 2014; Sai et al. 2020; van 't Hoff et al. 2020; Tychoniec et al. 2021). In the outermost region, nonaxisymmetric faint tails are also detected, as indicated by the dashed white arcs in the left panel of Figure 1. These tails are also seen in the continuum image in Tychoniec et al. (2021) and are consistent with the molecular line emission tracing the warped outer disk as well as the accretion flows (Yen et al. 2014; Sai et al. 2020; van 't Hoff et al. 2020).

The zoom-in view of the continuum image (middle panel of Figure 1) shows a central compact source at $\Box 0'$ 1 that is unresolved at the current angular resolution. The peak intensity We note that there is an additional uncertainty in the intensity's 5.4 mJy beam¹, which corresponds to a brightness scale of the CLEANed images due to the JvM effect (Jorsater temperature of 21 K using the full Planck function. This component is spatially unresolved even in the higher-resolution maps imaged with smallerrobust parameters (Appendix A), indicating that this component is quite compact ($\square 0 04$).

> Interestingly, an emission enhancement(i.e., a ring-like structure)is identified at a radius of ~0 4 from the central protostellar position (middle panel of Figure 1) he locations of the ring and the adjunctgap are marked by the solid and dashed white arcs, respectively, in the middle panel of Figure 1. A nonaxisymmetric brightness distribution (i.e., substructure in

^a Upper state energy of the transition.

b Taken from the Cologne Database for Molecular Spectroscopy (CDMS; Müller & 2011, 2005; Endres et al 2016).

Based on the Equation (7.7) in https://almascience.nao.ac.jp/documentsand-tools/cycle8/alma-technical-handbook.

²³ The self-calibration and imaging scripts forthis source are available at https://github.com/jjtobin/edisk.

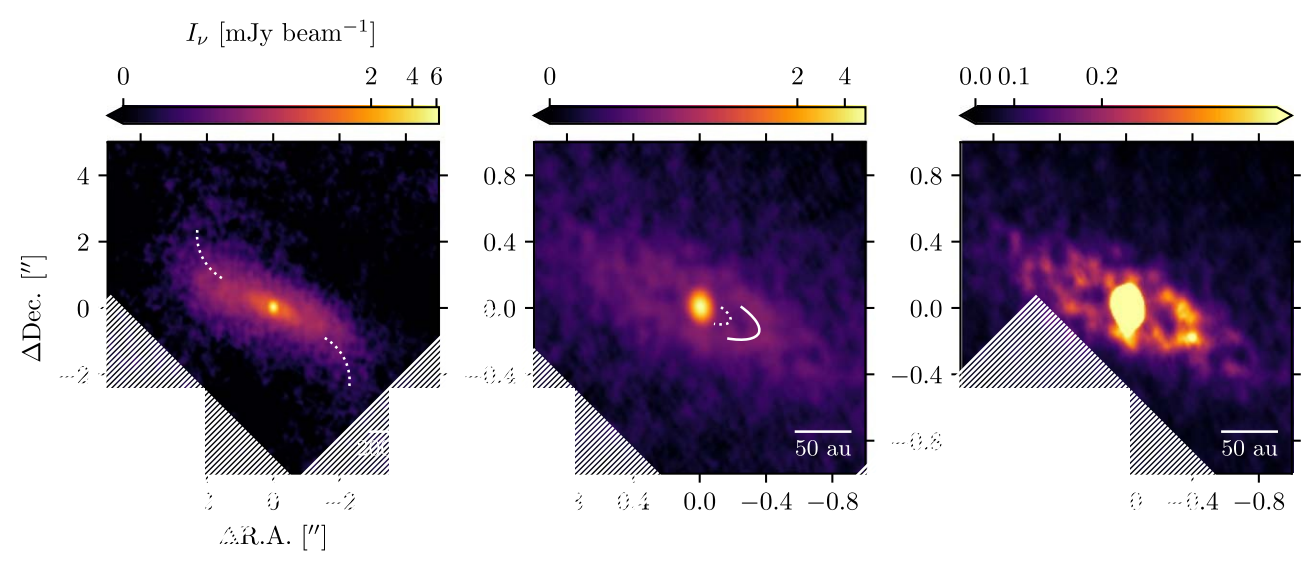


Figure 1. 1.3 mm continuum images ofthe disk around L1489 IRS. Left: large-scale view of the disk with robust = 2.0 and uvtaper = 1000 kλ. nonaxisymmetric feature appears in the outermost region as guided by the dashed white arcs. Center: zoom-in view of the disk with robust = 1.0. The locations of the ring and gap are indicated by solid and dashed white lines, respectively. The gap location is identified visually, while the ring location is based on the visibility analysis described in Section 4.1. For the left and center panels, the color scaling is stretched by an arcsinh function to accentuate features with low surface bright Right: same as the center panel, but with a limited color range stretched by a sinh function to accentuate the nonaxisymmetric feature at the ring. For each panel, to color scaling is saturated at 0.0 be beam size is represented by the white ellipse at the lower beful the white scale bars are plotted in the lower right corner.

the azimuthal direction) at the ring is also observed the right panel of Figure 1 shows the continuum image with an adjusted color scaling to clearly show the asymmetry. The western side of the ring is slightly brighter than its eastern counterpathte examine the properties of this ring-like structure in more detail in Section 4.1 and discuss its origin in Section 5.

two-component (i.e., central compact component and extendedunction of the blackbody radiation athe temperature TWe tenuous component) 2D Gaussian fit on the untapered continuum image using the imfit task in CASA. We note that due to the ring-like structure, the 2D Gaussian fityields residuals at a level of about 8σ at the ring location. The position of the emission peak of the central compact component derived by the fit is $\alpha(ICRS) = 04^{\circ}04^{\circ}43^{\circ}080$, $\delta(ICRS) = +26^{1}18^{m}56^{s}12$. This is used as the position of the central protostarin the following analysis. The deconvolved sizes of the compact and extended components are 0.037×0.024 (PA = 180°, ~5.4 ×~3.7 au) and 3.9×1.3 (PA = 66°, ~570 ×~190 au), respectively. The deconvolved size of the extended components consistent with previous observations (Yen et al. 2014; Sai et al. 2020). The inclination angle of the outer extended disk is estimated from the deconvolved size to be ~71° (0° for the face-on configuration) respectively. We note that these estimates re lower limits assuming a geometrically thin disk. The derived inclination angle is similar to the value measured by previous observation ptically thick. (73°; Sai et al. 2020). The total flux density originating from both components is 91 ± 9 mJy. The flux calibration uncertainty of 10% is added in quadraturene measured flux density is ~53% higher than that measured by Sai et al. (2020)velocity-integrated intensity (or zeroth moment), velocity (~59 mJy), which has been found to be due to the JvM effect (Jorsater & van Moorsel1995; Czekala etal. 2021; see also Section 2). Application of the JvM correction (Czekala et al. 2021) resulted in a JvM ò (the ratio of the CLEAN beam volume to the dirty beam volume) of ~0.26 and a similar flux

When we assume that the continuum emission al 25 GHz stems purely from the thermadust emission and is optically

density (~50 mJy) to that derived by Sai et a(2020).

thin, the total dust mass can be estimated by

$$M_{\text{dust}} = \frac{F_n d^2}{k_\rho B_\rho (I)},\tag{1}$$

where F_v is the flux density,d = 146 pc is the distance to the To quantify the overall emission properties, we performed a source κ_v is the dust mass opacity and $B_v(T)$ is the Planck adopted the flux density of 50 mJy from the JvM-corrected image and the dust mass opacity of=x2.3 cm² g⁻¹ based on Beckwith et al. (1990) with an assumption of the dust-to-gas mass ratio of 0.01Adopting dust temperatures of T = 20 K, a typical value used in Class II surveys (e.g., Andrews & Williams 2005: Ansdell et al. 2016: Tobin et al. 2020), and T = 58 K based on the prescription in Tobin et 42020),

$$T = 43 \left(\frac{L_{\text{bol}}}{1 L_{\square}} \right)^{1/4} \text{ K},$$
 (2)

with the bolometric luminosity of L_{bol} = 3.4 L_{e} (Ohashiet al. 2023), we obtain disk dust massesof 31 M_{\oplus} and 8.9 M_{\oplus} , because the emission at the central compact component may be

3.2. Molecular Lines

Figures 2 and 3 show the molecular line maps of the centroid, and peak brightness temperaturewith large-scale and zoom-in views. All the maps are generated using bettermoments (Teague & Foreman-Mackey 2018). For the velocity-integrated intensity mapsive integrate only the emission above 2oFor the velocity centroid maps and peak brightnesstemperature mapswe use the quadratic method implemented in bettermoments rather than traditional first/ eighth moments.

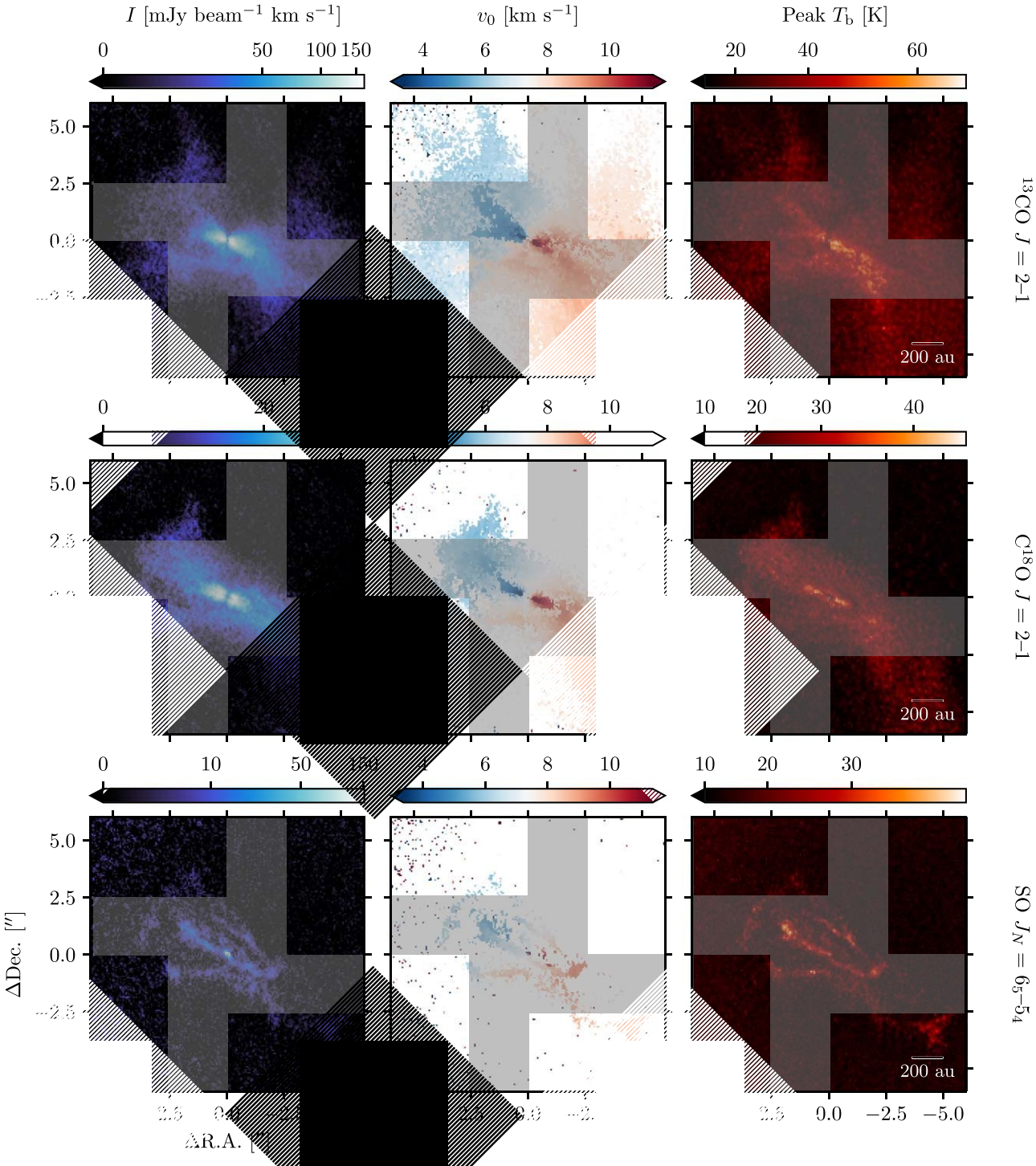
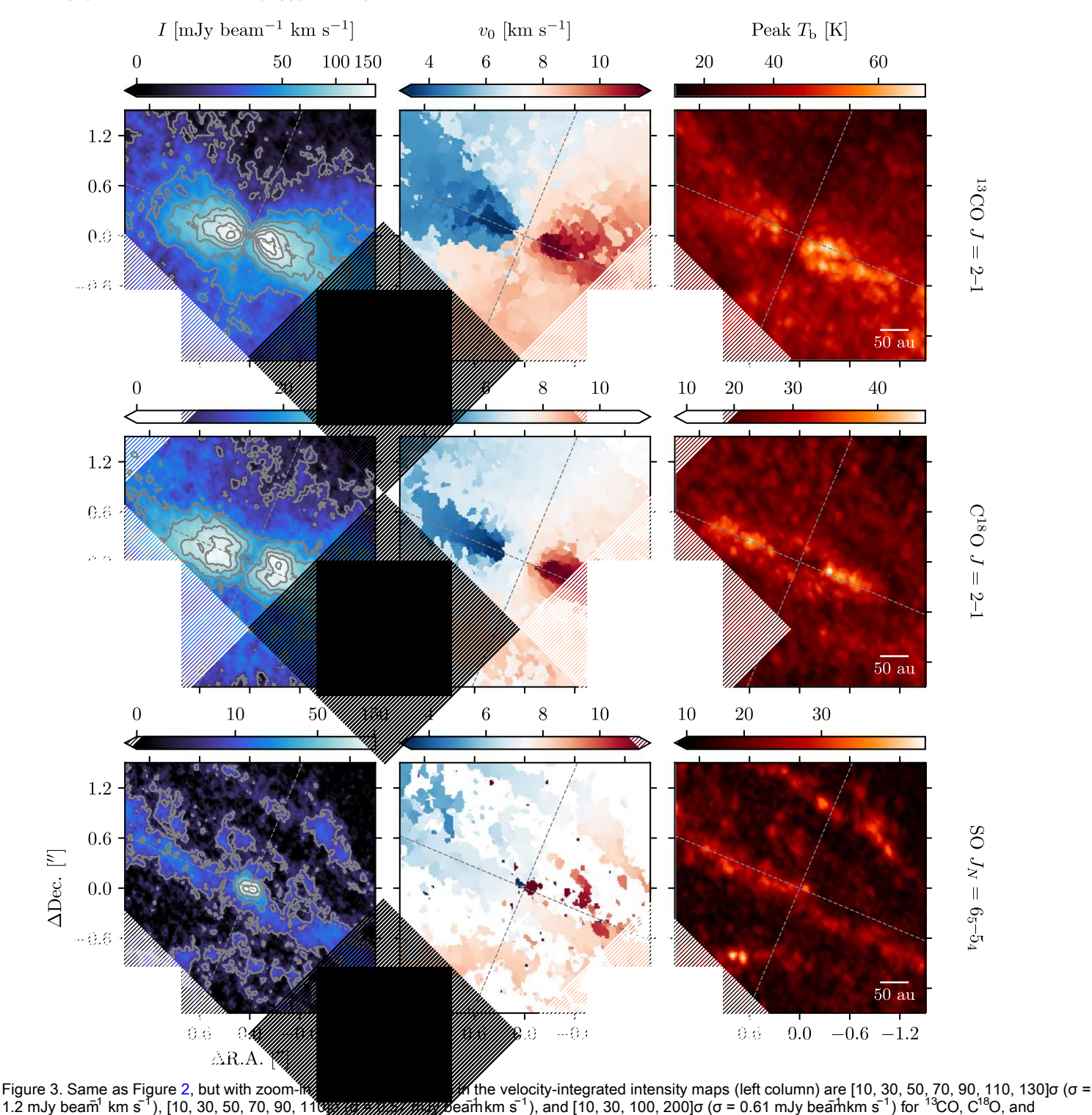


Figure 2. Velocity-integrated intensity maps oid maps (center columnand peak brightness temperature maps (right columnaction) oid maps (center columnaction) oid maps (ce J = 2-1 (top row), $C^{18}O$ J = 2-1 (center row), a^{18} attom row). The velocity centroid and peak brightness temperature maps are generated by the quadratic method implemented in bettermoments kity-integrated intensity maps, only emission higher than 2σ has been integrated. The color scaling quadratic method implemented in bettermoments of the color of the peak brightness temperature maps, the conversion from intensity to brightness temperature was not stretched by the arcsinh function and saturated at the peak brightness temperature maps, the conversion from intensity to brightness temperature was not stretched by the arcsinh function and saturated at the peak brightness temperature maps, the conversion from intensity to brightness temperature was not stretched by the arcsinh function and saturated at the peak brightness temperature maps. using the full Planck function. The color scaling is strettind by the sinh function and saturated at 10 K for visual clarity. For all panels, the synthesized beam is sho in the bottom left corner, while the scale bar in the bottom right corner indicates 200 au. The dashed gray lines indicate the direction of the major and minor axis of dust disk (PA =67° as derived by the visibility analysis described in Section 4.1).

3.2.1.13CO

systemic velocity is 7.38 km s¹, as derived by the velocity

structure analysis (Section 4.2). The velocity-integrated intensity map with a large-scaleview (top left panel of The maps of the 13 CO J = 2–1 emission are shown in Figures 2 and 3 (top rows). The emission is detected above 30 of the dust disk at r \square . 5, and the velocity centroid map (top in a velocity range from -0.2 to 15.6 km s $^{-1}$, where the middle panel of Figure 2) shows a rotation signature of the Figure 2) shows an elongated morphology along the major axis disk. In the outer region (r 2 15), the commission shows an



extended structuresuggesting that the ¹³CO emission traces originates from the surface of the inclined diskThe brighter emission on the southern side indicates that the southern s same transition and found a similar emission morphology (see the far side of the disk from which the emission of the warm Appendix C in their work).

SO, respectively.

The velocity-integrated intensity map with a zoom-in view (top left panel of Figure 3) shows bright, double-peakeco emission at a spatial scale of r ☐ 0 therestingly, the peaks of the ¹³CO emission are slightly shifted southward from the disk major axis. This would be evidence that the

originates from the surface of the inclined diskThe brighter emission on the southern side indicates that the southern side is the far side of the diskfrom which the emission of the warm disk surface reaches the observer directly (e.g., Lee et al. 2017; Ruíz-Rodríguez et al. 2017; Villenave et al. 2020; S. Takakuwa et al. 2023, in preparation). This configuration of the disk is consistentwith the outflow directions, where the red- and blueshifted robesare located on the northern and southern sides, respectively (Yen et al2014).

The top right panels of Figures 2 and 3 show the peak brightness temperature maps. The peak brightness temperature The maps of the SO ($J_N = 6$ 5–5₄) emission are shown in reaches \Box 60 K at r \Box 0′ 5, again suggesting that the \Box 13CO Figures 2 and 3 (bottom rows). The emission is detected above emission traces the disk surface where the temperature is higher over a wide velocity range from \neg 3.8 to 19.2 km s \Box 1. than in the midplane due to the heating by the protostar or the Overall, the morphology of the SO emission is different to one of the S accretion shock. The map also shows the higher brightness temperature on the southwestern (oredshifted)side, which may indicate a nonaxisymmetric temperature structure of the disk. The brighter molecular line emission on the southwestern and the diffuse extended emission in the outer diskhile the (or redshifted) side of the disk has also previously been observed in CO and HCO emission (van 't Hoff et al. 2020).

3.2.2.C18O

The maps of the $C^{18}O$ J = 2–1 emission are shown in Figures 2 and 3 (middle rows). The emission is detected above xtremely high velocities of ±10-12 km s⁻¹ with respect to 3σ in a velocity range from 0.8 to 12.8 km⁻³. The velocitylack of the C^8O emission in the innermost region (r \square 0 2). In emission exists. While the C18O emission shows the doublepeaked morphology atr ≈ 0.5 similar to that of ^{13}CO , no significantshifts of the peaks from the major axis of the disk are seen, in contrast to the velocity-integrated intensity map of traces the rotating disk (bottom middle panef Figure 2). In ¹³CO (top left panel of Figure 3). This indicates that the ⁸O emission mainly traces the gas near the disk midplane. Moreover, the radii of the C¹⁸O peaks are slightly larger than those of the ³CO peaks, which is more clearly presented in the radial intensity profiles in Section 3.3.

In the outer region (1.75 \square r \square 4"),a warped structure is seen, in which the redshifted part is curved toward the southwest and the blueshifted part toward the northeast (Figure 2). This feature was firstfound by Sai et al. (2020), who interpreted it as a misaligned Keplerian disk based on the emission shows lowerpeak brightness temperature. In the emission shows lowerpeak brightness temperature. It is is velocity structure analysis. Furthermore, extended redshifted emission is presentin the outermost region (r \square 4") of the southwestern (redshifted)ide (see the middle left panel of Figure 2), consistent with the infalling accretion flow observed in Yen et al. (2014). The blushifted conuterpart of this component is also seen as a slight extension to the north on the ontinuum and molecular lines; espectively. The method we northeastern side.

the highest velocity (±3–5 km⁻³ with respect to the systemic velocity) along the major axis of the disksuggesting that the high-velocity component of the component of the the rotating disk. A similar velocity structure was observed by the highest-velocity component, which is due to the absence of azimuthal substructures for the continuum and each line the disk emission (possibly caused by the actugates absence and/or the continuum oversubtraction; see Section 5.1), as seethe radial profiles is made in Section 5. in the velocity-integrated intensity map (middle lefbanel of

The peak brightness temperature map (the middle right panetenuous extended disk emissiom addition to these compoof Figure 3) also suggests thathe C¹⁸O emission originates are located close to the disk major axis. Similar to the velocity-the southwestern side is brighter that ring position than that integrated intensity map (the middle left panel of Figure 3), the extracted from the northeastern side by 0.08 mJy beams. and a ring-like structure with a radial peak at r ~ 0.4. In addition, the southwestern (oredshifted)side of the disk is slightly brighter than the northeastern side, consistent with the shoulder-like structures are tentatively identified at 5 (or

3.2.3.SO

that of ¹³CO and C¹⁸O. The velocity-integrated intensity map with the zoom-in view (bottom left panel of Figure 3) exhibits a prominent compact emission in the innermost region ($t' \square 02$) diffuse SO emission lacks the high-velocity componentat $r \approx 0.2-1$ " seen in ^{13}CO and $C^{18}O$ (see the middle column of Figure 3). The central compact emission is marginally spatially resolved and shows an elongated structure along the east-west direction. Interestingly, this emission component shows a velocity gradient along the elongation direction over the the systemic velocity (bottom middle panel Figure 3). The integrated intensity map (middle left panel of Figure 3) shows aprigin of this emission is discussed in detail in Section 5.5. The outer diffuse emission shows a complex structure in which the the intermediate region (0 2 🗆 r 🖾 1 5), an elongated disk-likeemission is mainly distributed along the major axis of the disk as well as in the regions relocated from the axis (bottom left panel of Figure 2). It also shows the velocity gradient along a direction similar to the major axis of the disk that partially addition, an SO emission clump is detected on the southwestern side of the disk ($r \approx 6''$), consistent with previous observations (Yen et al. 2014).

> The peak brightness temperature map office SO emission (bottom right panels of Figures 2 and 3) is highly intriguing. The multiple local enhancementsof the peak brightness temperatureare identified in the outer region. They may indicate the localenhancement fthe gas temperature due to the accretion shockOn the other hand, the central compact discussed in more detail in Section 5.5.

3.3. Radial Intensity Profiles

Figures 4 and 5 show the radial intensity profiles of the used to generate these radial rofiles is described in detailn The centroid velocity map (central panel of Figure 3) shows Appendix B. Briefly, we averaged the emission ovecertain radial bins within the limited wedge of ±45° with respect to the disk major axis. In addition to the profiles averaged over both sides of the disk, we calculated the profiles extracted from each southwestern (redshifted)ide and northeastern (blueshifted) Sai et al. (2020). In the innermost region (0 2), the map lackside of the disk to show the azimuthal variations. The radial and emission are described below. more detailed comparison of

Continuum—Figure4 shows that the continuum emission consists of the centrally peaked compactomponent and the nents, a gap-ring pair is identified at /~0 2 (or 30 au) and ~0 4 from the disk midplane because the peak emission component for 60 au) radii from the disk center. The profile extracted from peak brightness temperature also shows a central dip at4r □ 0≈10σ significance), which can be seen more clearly in the inset panel of the leftpanel of Figure 4.In the radial profile of the robust =2.0 tapered image (right panel of Figure 4), two distributions of the 3 CO peak brightness temperature structure. 220 au) and $\approx 2'$ 3 (or 340 au). The profiles also show slight

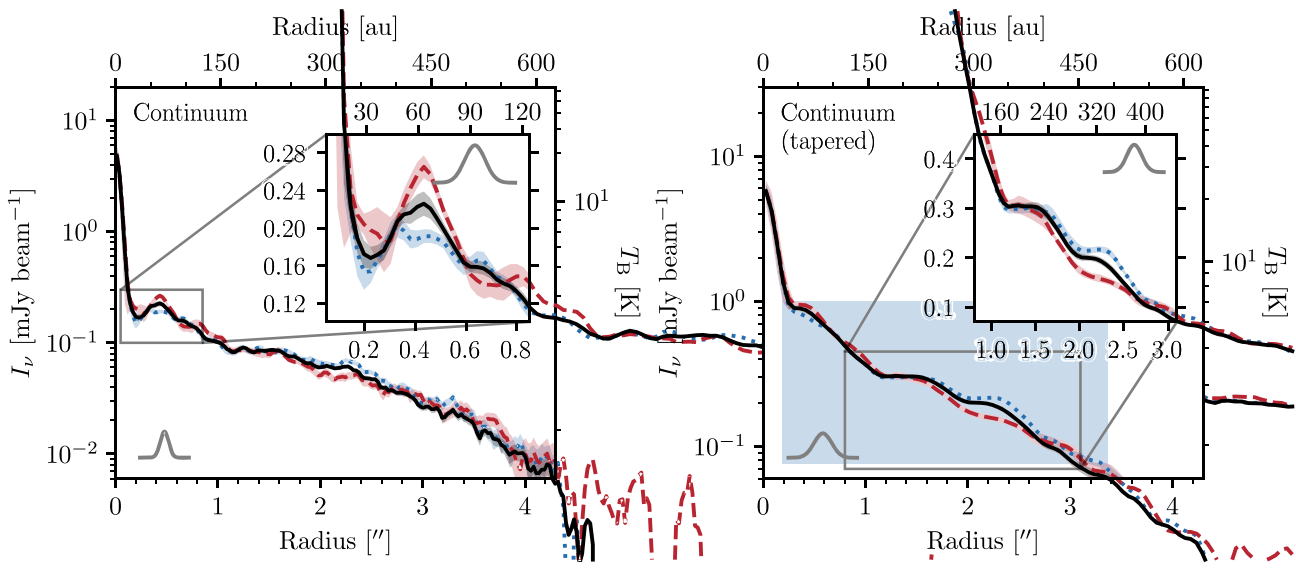


Figure 4. Deprojected azimuthally averaged radial intensity profiles of the 1.3 mm continuum. The left panel presents the radial profile of the image with robust =1.0, and the right panel shows the radial profile of the robust =2.0 tapered image. The dashed red and dotted blue lines represent the profiles extracted from the southwestern (redshifted) side and the northeastern (blueshifted) side of the disk, respectively. The solid black line shows the profile averaged over both sides of the disk. These profiles are computed by averaging over ±45° wedges with respect to the disk major axis (PA =67°). The shaded regions indicate 1σ scatter at each ra bin (see Appendix B). In the inset of each panel, the zoom-in views of the innermost ring (left panel) and outer shoulders (right panel) are shown, respectively. The Gaussian profile in the lower left corner of each panel and the upper right corner of the inset indicates the width of the major axis of the synthesized beam. The right vertical axis indicates the brightness temperature yerted from the intensity using the full Planck function.

variations between the southwestern side and the northeasterrposition-velocity (PV) diagram of the C18O emission to side at these shoulder-like substructures. The northeastern sidenvestigate the nature of the disk rotation (Section 4.2). is brighter than the southwestern side.

¹³CO J = 2–1—The radial intensity profile extracted from both sides peaks at 40 2 (or 30 au) radii. Additionally, a subtle shoulder is identified at ~! 3 (or 190 au) radii. This feature is also seen in the profiles extracted from the southwestern and northeastern sidesof the disk, although the feature in the northeastern side is subtleOverall, the southwestern side is brighter than the northeastern side, while the difference is more significant in the outer radii (□'08).

 $C^{18}O$ J = 2–1—The peak of the $C^{18}O$ intensity profile is slightly shifted outward (≈0 4 or 60 au) compared to the peak of 13CO. From this peak, the C18O profile shows a steep decline until $r \approx 1.4$ (or 200 au). At $r \approx 2.2$, the C¹⁸O intensity profile from the southwestern side shows a slight enhancement, which is brighter than the emission on the northeastern side. While the D profiles show the difference between the southwestern and northeastern sides of the disk in the outer region (r \sum "!1 5 or 220 au), the profiles are consistent in the inner disk (r \square 1/1 5).

SO $J_N = 6_5 - 5_4$ —The SO emission is centrally peaked at r □ 0'2, although the innermostbin shows a slight central depression (the inset of the right panel of Figure 5). The extent radial coordinate r is the disk coordinate deprojected with the of the central compact component is up td'≈0 2. In addition to the central compact component, there is a tenuous diffuse emission, as also seen in the maps (Figure 2). There is no major variation between the southwestern and northeastern sides, although the 2D emission distributions are complex (Figure 2).

4. Analysis

We performed two simple modeling approaches to the observed continuum and line emission: (1) an analytical model similarly given by fit to the observed continuum emission in the visibility domain to characterize the radial substructures and geometry of the dusty disk (Section □4.1and (2) a rotation curve fit to the

4.1. Visibility Analysis of the Dust Continuum Emission

To precisely characterizethe dust disk geometry and morphology, we conduct an analytic model fit to the observed dust continuum data in the visibility domain. A visibility analysis has two advantages over the image analysis. First, the uncertainties associated with imaging can be avoided. Second, the visibility can probe the structures on scales smaller than the beam size of the image, although the smallest scale that can be probed is limited by the maximum baseline lengthWe only consider the axisymmetric componeated the innermostlust ring becausethe nonaxisymmetriccomponents and outer shoulder-like structures are rathefiaint. We use a Gaussian ring model with an intensity distribution given by

$$I_{r,r}(r) = I_{r,r} \exp\left(-\frac{(r - r_{0,r})^2}{2W_r^2}\right),$$
 (3)

where \downarrow_{r} is the peak intensity of the ring component, is the radius of the ring centerand w is the width of the ring. The position angle (PA) and the inclination angle (i) The central

$$I_{\text{AC}}(r) = I_{\text{AC}} \exp\left(-\frac{r^2}{2W_c^2}\right). \tag{4}$$

We add the extended disk component as a Gaussiand, it is

$$I_{n,e}(r) = I_{n,e} \exp\left(-\frac{r^2}{2W_e^2}\right).$$
 (5)

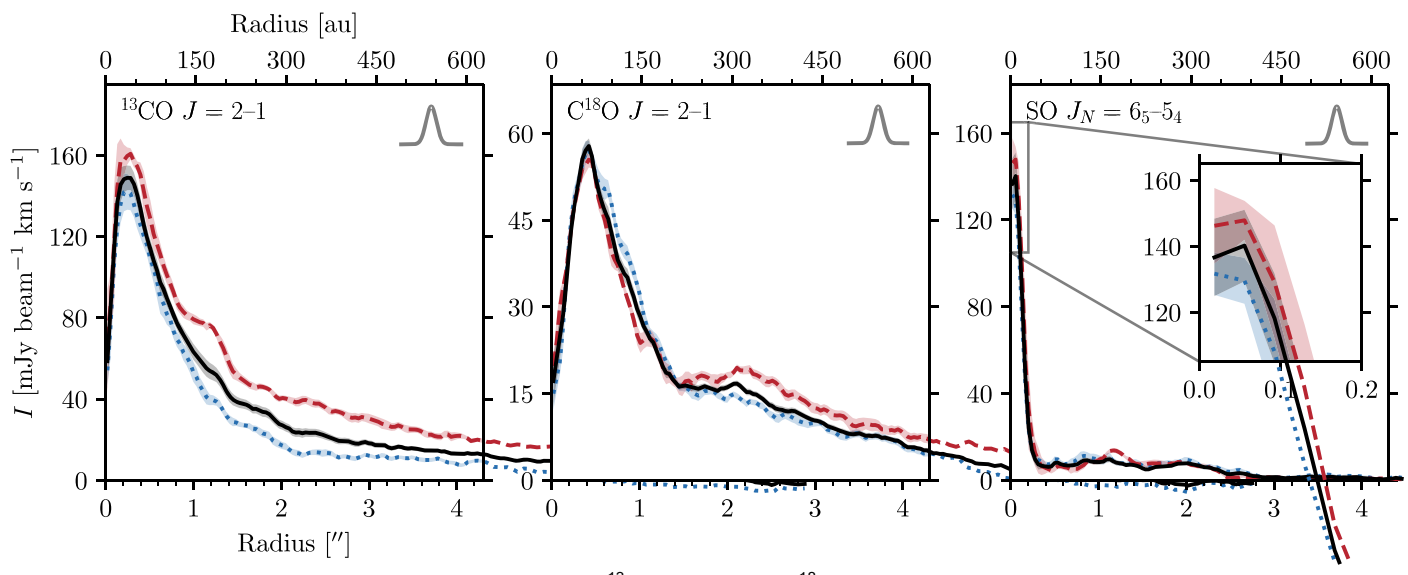


Figure 5. Deprojected azimuthally averaged radial intensity profile 300 J = 2-1 (left), C¹⁸O J = 2-1 (middle), and SO_NJ = 6₅-5₄ (right). While the dashed red and dotted blue lines represent the profiles extracted from the southwestern (redshifted) side and the northeastern (blueshifted) side of the disk, respectively, the s black line shows the profile extracted from both sides of the disk. These profiles are computed by averaging over ±45° wedges with respect to the disk major axis (=67°). The shaded regions indicate 1σ scatter at each radial bin (see Appendix B). The Gaussian profile in the upper right corner of each panel indicates the width the major axis of the synthesized bearthe inset of the right panel shows the slight central depression of the SO emission.

The full model is then given by the sum of all the components.

$$I_{n}(r) = I_{n,r}(r) + I_{n,c}(r) + I_{n,e}(r)$$
 (6)

We directly fit this model to the observed visibilities. We used the flux density (F*) instead of the peak intensity (**) for the parametersin practice. First, the model image is generated in the image plane and is then Fourier-transformed by the GALARIO code (Tazzari et al. 2018) onto the observed sampling of the (u,v) plane. We also consider the disk center offset from the phase center of the observationsesulting in additional parameters of (x_0, y_0) . In total, we consider 11 parameters $\hat{q} = \{F_{\alpha,n}, w_r, F_{\alpha,r}, F_{\alpha,r}, w_c, F_{\alpha,e}, w_e, PA, i, x_0, y_0\}$, and search the parameter space with the Markov chain Monte Carlo (MCMC) method using the emcee package (Foreman-Mackey et al. 2013). The parameter space is sampled by 200 walkers with 1000 steps, and the initial 700 steps are discarded as burn-in.

Table 2 summarizes the resultaparameters of the fitWe find a PA of 67° and an inclination of 72° both of which are consistentwith the 2D Gaussian fit on the image plane (see Section 3). The ring radius is estimated to be 30 (or 56 au), which is consistent with the peak of the radial intensity profile (Figure 4). The ring width is 0/24 (or 35 au). The size of the central compact component is derived to b\(\text{b} \(\text{0} \) 0073 (or 1 au), which is smaller than the deconvolved size derived by the 2D Gaussian fit on the image plane (see Section 3). This indicates that the central componentis indeed very compact and not spatially resolved at the current resolution. The size of the extended componen(1"58 in the standard deviation of the Gaussian, or 3 72 in FWHM) is comparable to that derived by observations and the model both real and imaginary parts JvM-corrected image (which is expected to recover the correctthe largestspatial scale (which can be traced by the present flux scale; see Section 3).

The comparison of the best-fit model (i.e., the model that maximizes the likelihood) with the observed visibilities (deprojected and azimuthally averaged) is shown in Figure 6. Overall, the observed visibilities are reproduced welly the

Table 2 Best-fit Parameters of the Visibility Fit

F _{v,c} mJy Flux density of the central compact component w _c "Size of the central compact component F _{v,r} mJy Flux density of the ring component F _{v,r} "Width of the ring 0.2 r _{0,r} "Radius of the ring location 0.3 F _{v,e} mJy Flux density of the extended 4 component w _e "Size of the extended component 1. PA Position angle of the disk measured from north to east d "Inclination angle of the disk (0° for face-on) x ₀ "Source offset from the phase center 0.000 along R.A.		*		
$\begin{array}{cccccccccccccccccccccccccccccccccccc$	Value	tion	Unit	Parameter
w _c Size of the central compact 0.00 component F _{v,r} mJy Flux density of the ring component 5. w _r "Width of the ring 0.2 r _{0,r} "Radius of the ring location 0.3 F _{v,e} mJy Flux density of the extended 4 component w _e "Size of the extended component 1. PA °Position angle of the disk measured from north to east inclination angle of the disk (0° for face-on) x ₀ "Source offset from the phase center 0.000 along R.A.	5.05 0.04	•	mJy	F _{v,c}
w _r " Width of the ring 0.2 r _{0,r} " Radius of the ring location 0.3 F _{v,e} mJy Flux density of the extended 4 component 1. PA " Size of the extended component 1. PA " Position angle of the disk measured from north to east 6 id " Inclination angle of the disk (0° for face-on) 7. x ₀ " Source offset from the phase center along R.A. 0.00	0.0072 2 0.00024	·	"	W _C
$\begin{array}{cccccccccccccccccccccccccccccccccccc$	$5.39^{+0.22}_{-0.22}$	nsity of the ring component	mJy	$F_{v,r}$
F _{v,e} mJy Flux density of the extended component We " Size of the extended component 1. PA Position angle of the disk measured from north to east id Inclination angle of the disk (0° for face-on) x ₀ " Source offset from the phase center along R.A.	$0.238^{+0.016}_{-0.016}$	f the ring	"	W_{Γ}
component we "Size of the extended component 1. PA Position angle of the disk measured 6 from north to east id Inclination angle of the disk (0° for 7. face-on) x ₀ "Source offset from the phase center 0.000 along R.A.	$0.384^{+0.018}_{-0.019}$	of the ring location	"	$r_{0,r}$
PA ° Position angle of the disk measured 6 from north to east id ° Inclination angle of the disk (0° for face-on) x ₀ ″ Source offset from the phase center 0.000 along R.A.	41.4 ⁺ 0.4 0.4	•	mJy	$F_{v,e}$
from north to east ig 'Inclination angle of the disk (0° for 70 face-on) x ₀ '' Source offset from the phase center 0.000 along R.A.	1.58 ^{+ 0.02}	he extended component	"	We
face-on) x ₀ " Source offset from the phase center 0.000 along R.A.	67.0 ⁺ 0.3	· ·	o	PA
along R.A.	72.0 ⁺ 0.2 0.3	,	0	ď
y ₀ Source offset from the phase center 0.00	0.0088† ^{0.00010}	·	"	x ₀
along decl.	0.0010 [†] 0.00015 0.00016	•	"	Уо

Note

model. Importantly, a dip at ~200 kλ (the inset of Figure 6) clearly indicates the presence of ring-like structure. In the shortest-baselinebin, a slight discrepancy between the the 2D Gaussian fit. The total flux density (summed over all thexists, although it is within the uncertainty. The discrepancy in components) of 52 mJy is similar to the value derived from the the real part indicates that additional emission component(s) in observations) may be required to better reproduce the observations. The discrepancy in the imaginary part in the shortest-baseline bin suggests that the additional component(s) would be nonaxisymmetric with respecto the phase center. The potential presence of a large-scale nonaxisymmetric

^a The uncertainties correspond to the 16th and 84th percentiles of the posterior distributions.

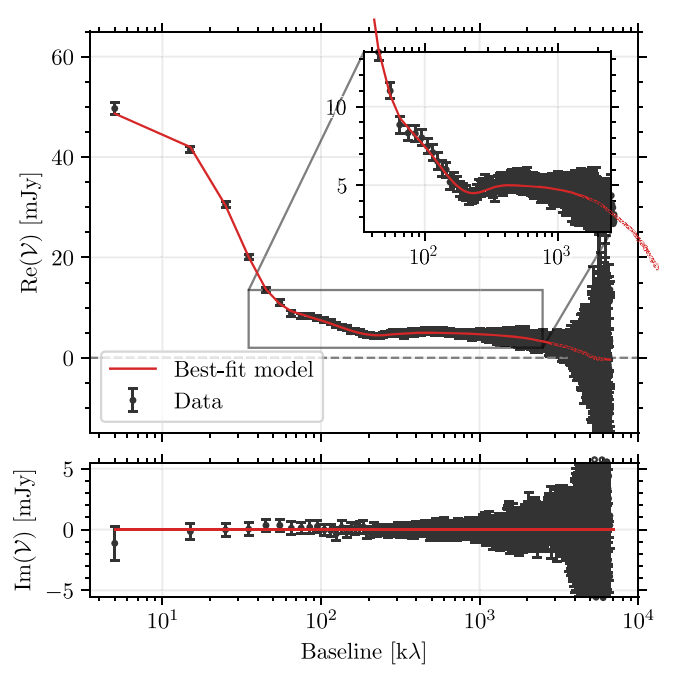
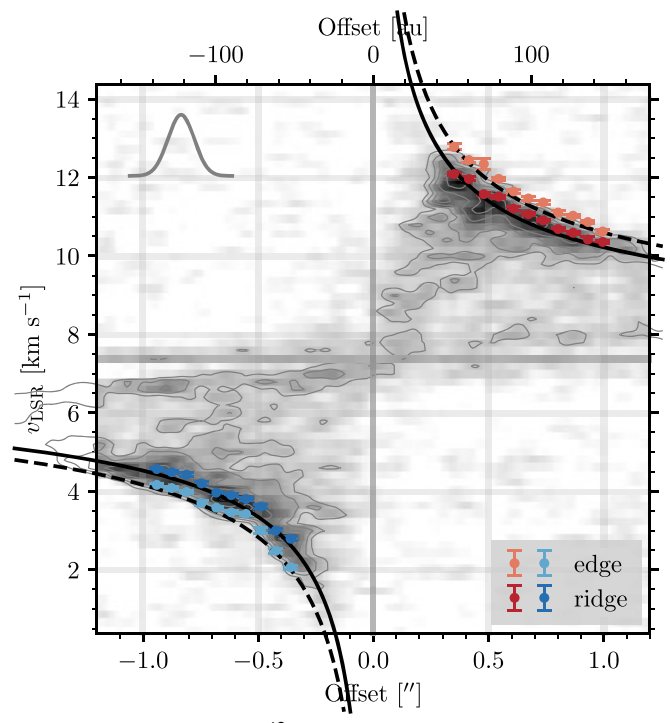


Figure 6. Comparison of the deprojected azimuthally averaged observed visibilities (black) and the best-fitmodel (red). The upper and lowerpanels show the real and imaginary parts, respectively. The zoom-in view of the long-Figure 7. PV diagram of the CO J = 2-1 emission along the disk major axis baseline regime is shown in the inset in the upper panel.

structure is consistent with the faint tails in the outermost region seen in the dust continuum image (left panel of Figure 1), which are not included in the current model.

4.2. Velocity Structure Traced by the ¹[®]O Emission

To investigate the velocity structure of the disk and infer the dynamical stellar mass, we use the O emission because the emission morphology suggests that traces the rotating gas near the midplane (see the middle lessanel of Figure 3). Sai et al. (2020) found a large Keplerian disk that extends to r ~ 600 au with a warped structure at r ~ 200 au by conducting region to avoid spatialresolution effects as described in the the power-law fitting to the data points derived from the PV diagram of C⁸O J = 2-1, and estimated a central stellar mass of 1.64 ± 0.12 Mg (see also Yen et al. 2014). We here independently verify the Keplerian rotation of the disk and estimate the central stellar mass using the Spectral Line Analysis/Modeling (SLAM) code (Aso etal. 2015; Sai et al. 2020, and references therein; Aso & Sai 2023). We follow the method described in Ohasleit al. (2023). First, the C18O PV diagram along the major axis of the dusty disk (PA =67° as derived by the visibility analysis; see Section 4.1) is generated data points: It is shown in Figure 7. The representative data point pairs (r, v) are extracted from the diagram, to which a power-law function $(v \propto r^{-p})$ is subsequently fitted. To extract the representative data points, we identified a peak velocity channel for each pixel where vlos is the line-of-sight component of the rotation of the positional axis and subsequently fit Gaussian to the adjacenttwo channels (i.e., three channels in total). This is referred to as the ridge method (e.g., Yen et al. 2013; Lee et al. the systemic velocity. The free parameters are and very the 2018; Sai et al. 2020; see also Aso & Machida 2020). As a complementary methodie extracted the points awhich the emission reaches 5σ for each pixel of the positional axis, which visibility analysis described in Section 4.1. To search the is referred to as the edge method (e.g.Seifried et al. 2016; Alves et al. 2017; see also Aso & Machida 2020). The two methods result in different estimates of the central stellar massWe ran 1000 steps with 200 walkers and discarded the initial



(PA = 67°). The contours are drawn from 5σ to 15σ in steps of 2σ , where σ = 1.7 mJy beam⁻¹. The derived data points from the PV diagram by SLAM are indicated by red/blue circles (ridge method) and orange/light blue circles (edge method)The solid and dashed black lines represent the rotation curve, with the best-fit parameters listed in Table 3 for data points derived from the ridge and edge methods, respectively. The systemic velocity derived from both fits (averaged best-fitvalues; 7.375 km s⁻¹) is indicated by the horizontal dashed gray line. The Gaussian profile in the upper left corner indicates the size of the major axis of the synthesized beam.

overestimate it, depending on the spatial resolution (Maret et al. 2020). The difference between the central stellar masses derived from these methods is thus adopted as a systematic uncertainty. In addition, we only used the $r = \pm 0.13-1.10$ Appendix of Aso et al. (2015), and substructure (i.e., the central depression and the warped structure at r □ 200 au). The extracted representative data points are shown as red and blue points in Figure 7. We verified that these data points follow Keplerian rotation by conducting a power-law fit to them with SLAM. The best-fit power-law indices p are 0.480 0.008 and 0.495 0.008 for the ridge and edge methods, respectively, the index p \approx 0.5 is consistent with Keplerian rotation. To infer the central stellar mass, we fit the Keplerian rotation model to these

$$V_{\text{los}} = \sqrt{\frac{GM_{\text{l}}}{r}} \sin(i) + V_{\text{sys}}$$
 (7)

velocity, G is the gravitational constant is the central stellar mass, r is the radius, i is the disk inclination angle, and is disk inclination angle is fixed to 72° as derived from the parameterspace, the MCMC algorithm implemented in the emcee package (Foreman-Mackey at. 2013) was adopted. the ridge method can underestimate and the edge method can 500 steps as burn-in. The convergencewas tested by an

Table 3 Results of the Keplerian Fits to the ¹⁶O PV Diagram

Method	M _å (M _e)	V _{sys} (km s ⁻¹)
ridge edge	1.498 0.008 1.911 0.009	7.372 0.009 7.377 0.010 7.377 0.010

Note. The uncertainties correspond to the 16th and 84th percentiles of the posterior distributions.

autocorrelation analysis. The best-fit values (median of the posterior distributions) and uncertainties (16th and 84th percentiles)are reported in Table 3 for the ridge and edge methods.

the two methods, the best-fit stellar masses are significantly different (Table 3). The value from the edge method is higher than that from the other method which is natural as the edge method tends to trace a higher velocity than the ridge method ap structures in the dustemission is the dustgrowth front, each pixel. Thus, the derived stellar mass including the systemic uncertainty is 1.5-1.9 Mg. This is consistent with the previous estimates of 1.64 ± 0.12 Nby Sai et al. (2020), who used the ridge method and the data points from the outer warped disk as well.

5. Discussion

5.1. Origin of the Dust Ring

As described in Section 3,our observations have detected several radial substructuresin both dust continuum and molecular line emission. Various mechanismshave been suggested as the origin of ring/gap structures in protoplanetary protostellar disks well (Ohashi et a2021, 2022a), suggesting disks: e.g., planet-disk interaction (e.g. Zhang et al. 2018), modification of the dust grain properties at the snowlines of volatiles (Zhang et al. 2015; Okuzumi et al. 2016), disk winds (e.g., Takahashi & Muto 2018), and dust growth (Ohashi et al. 2021).

If the dust ring at ~57 au is carved by a planet, the gas will also show a ring-gap structure at similar radius. To explore the gas and dustiructures around the dusing, we compare the radial profiles of the dustcontinuum and line emission in the innermost region in Figure 8 (left panel). Interestingly, the dust ring and the radial peak of the C18O intensity profile coincide. Because the C⁸O emission is likely to trace the region near the midplane based on the emission morphology of section 4.2, $\zeta_d = 0.01$, and $t_{disk} = (3-8) \times 10^4$ yr (Sai et al. the velocity-integrated emission map (Figure 3), this coincidence may indicate the presence of ring-like structure in both dust and gas. In the adjacent dust gap (at ≈30 au), the ¹³CO emission is bright, which is likely due to its optically thick emission at the disk surface, as indicated by the morphology on the velocity-integrated intensity map (Figure 3). While the dust and C¹⁸O intensity profiles at r

30 au show a similar behaviothe C¹⁸O intensity profile monotonically decreases inward at □ 30 auwhere the dust intensity profile shows a rapid increase. The 13CO intensity profile also shows a rapid decrease at □ 20 au. These are likely due to the continuum oversubtraction (e.g., Weaver et al. sure the spectral indices across the dust ring. the gas gap, while the coincidence of the dust ring and the radial peak of the C⁸O emission is likely real.

If we assume that the gas disk has a gap with the same depth as the dustgap and thatit is carved by a formed planet, the mass of the planet Mcan be estimated using

$$M_{\rm p} = 5 \cdot 10^{-4} \left(\frac{1}{\rm S_p/S_0} - 1 \right)^{1/2} \left(\frac{h_{\rm p}}{0.1} \right)^{5/2} \left(\frac{a}{10^{-3}} \right)^{1/2} M_{\rm B},$$
 (8)

where Σ_{D}/Σ_{0} is the surface density contrast (i.e., gap depth), h is the disk aspect ratio (i.e., the ratio of the scale height to the disk radius), α is the turbulence parameterand Ma is the central stellar mass (Kanagawa et al. 2015). If we adopt the contrast of 0.64 as measured on the dust intensity profile ethods. (Figure 4; assuming the emission is optically thin) as $_{p}\Sigma_{0}$, and assume h=0.05-0.1, $\alpha=10^{-4}-10^{-2}$, and the central stellar mass of 1.5-1.9 Mas derived in Section 4.2, the mass of the planet (if present) would be ~0.033-2.4 M

> Another possible mechanism to explain the innermost ring/ which was recently proposed by Ohashet al. (2021). They calculated the time evolution of the dustize distribution and surface density profile considering the grain growth via coagulation and radialdrift of dust grains and found that a ring-like structure in the surface density profile is formed at the dust growth front (or pebble production line;Lambrechts & Johansen 2014). Outside the dust growth front, the dust particles have not grown and remain in their initial states (micrometersize), while inside the growth front, they have grown to millimeter size or larger and drifted radially, resulting in a local maximum of the surface density profile (i.e., ring-like structure) at the growth front. The expected radiabcation of the ring matched the observed dusting locations in young that the dust growth front mechanism might explain the origin of dust rings, particularly in young disksOhashi et al.(2021) constructed an equation that predicts the radial location of the ring that is formed by this mechanism based on radiative transfermodeling. The important parameters that ontrol the location of the dust ring (R) are the disk age (t_{kk}), the stellar mass (M), and the dust-to-gas mass ratio_ι(ζ

$$R_{\rm c} = 56 \left(\frac{M_{\odot}}{M_{\odot}}\right)^{1/3} \left(\frac{Z_{\rm d}}{0.01}\right)^{2/3} \left(\frac{t_{\rm disk}}{0.1 \,\text{Myr}}\right)^{2/3} \,\text{au}.$$
 (9)

If we adopt a stellar mass of 1.5-1.9 Me as derived in 2022), the expected location of the dust ring is 28-59 aune ring location of 56 au found in our observations is consistent with this expectation. Ohashi et al. (2022a) also tentatively detected the ring-like structure at~90 au in the L1489 IRS disk; the difference with our result is likely due to their coarser spatial resolution. If the dust ring is produced by the dust growth front mechanism, dust grains in the inner □60 au have already grown to millimeter size or even larger (Ohastial. 2021). To confirm that grain growth has indeed taken place, higher-resolution multiband observations are needed to mea-

2018), which makes it difficult to infer the presence/absence of The observed ring/gap structure may also be formed by the inner misaligned disk. We discuss this possibility in Section 5.6.

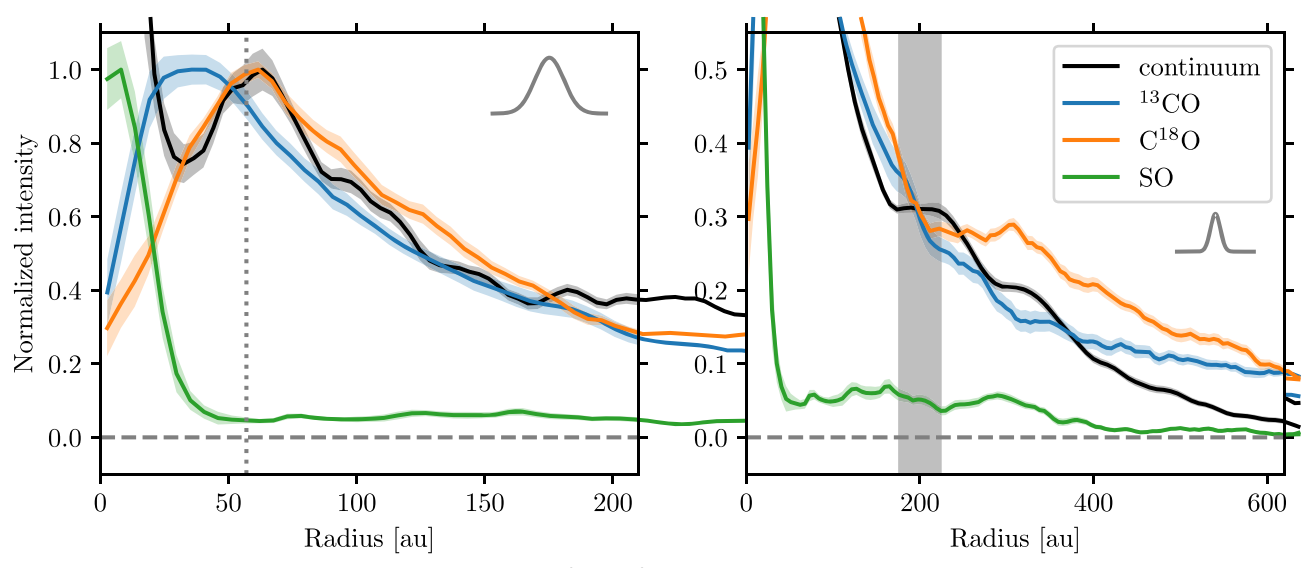


Figure 8. Comparison of the radial intensity profiles of the continuideo, C180, and SO. While the left panel shows the profiles in the innermost region, the right panel presents the outer region. The profiles of line emission are normalized by the radial peaks, while the continuum profile is normalized by the intensity at the profiles of line emission are normalized by the radial peaks, while the continuum profile is normalized by the intensity at the profiles of line emission are normalized by the radial peaks, while the continuum profile is normalized by the intensity at the profiles of line emission are normalized by the radial peaks, while the continuum profile is normalized by the intensity at the profiles of line emission are normalized by the radial peaks. of the ring. The horizontal dashed line represents the zero-intensity levels. In the left panel, the vertical dotted line indicates the position of the innermost dust ring, while the vertical gray shaded region in the right panel marks the position of the CO snowline inferred by Sai(@0a0).

5.2. Outer Disk Structures

In addition to the dust ring at 56 au, we identified two shoulder-like structures in the outer disk in the radial profile of the dust continuum (Figure 4). The comparison of the radial intensity profiles of the dust continuum and line emission in the outer region is shown in the right panel of Figure 8. The inner shoulder at~220 au coincides with the CO snowline location based on the radiative transfer modeling by Sai et al. (2020). The rapid inward increase in the C¹⁸O profiles at the shoulder also indicates the sublimation of CO molecules. Similar behaviors of CO line intensity profiles have been observed in Class II disks as well (e.g., Zhang et al.2021). While the coincidence between the dust shoulder and the CO snowline may imply a change in the dust property to form the substructured is also possible that the rapid increase in the radial profiles of the CO isotopologs might simply be due to the gas density enhancement.We also note that the shoulder radius of ~200 au coincides with the warped structuræs revealed by the C¹⁸O emission (Section 3.2.2; see also Sai et al2020)

The outer shoulder at ~340 au is located in the outer warpedevidence thathe dust grains are flared but not settled to the disk. At the same location, the © emission, which is located near the disk midplane, exhibits a subtle emission enhancement. Similar enhancements ofhe line emission have been observed in $C^{18}O$ J = 2–1 by Sai et al. (2020) and in $C^{17}O$ J = 2-1 by van 't Hoff et al. (2020). This may imply that CO depletion is much less significandutside ~340 au, which we call the secondary CO snowlineAs the disk column density decreases with radius hotodesorption due to penetrating UV radiation could keep CO in the gas phase outside a certain radius. A similar re-enhancement of the line emission at an outer radius is also observed in severalisks (Dutrey et al. 2017; Flores et al. 2021; Lin et al. 2023). In Class II disks, the double emission rings of DCOwhich is expected to trace the gas-phase CO (Öberg et al015; Cataldi et al2021).

5.3. Azimuthal Asymmetry

In addition to the radial substructures the dust continuum and molecular line emission also show azimuthal asymmetries (Section 3). As for the dust continuum, the southwestern side of the disk is brighter than the northeastern side in the duistig (see the right panel of Figure 1). Nonaxisymmetricdust emission has been observed in a handful of disks of both Class 0/I and Class II (e.g., van der Marel et al. 2013; Sheehan et al. 2020), at least part of which is considered to be nonaxisymmetric dust traps, e.g., vortices. In the L1489 IRS disk, the ring at ~56 au may thus have the dust trap (i.e., gas pressure maximum) on the southwestern side. Alternatively, the azimuthal variance in the temperature can also lead to the asymmetry of the dust emission, which might be caused by an inner misaligned disk (see Section 5.6).

The L1489 IRS disk shows an asymmetry of the dust continuum emission along the major axis (see the left panel of Figure 1). This is in contrast to several other eDisk sources that exhibit asymmetries along the disk minor axis (see Ohashi et al. 2023, for a gallery of the continuum images). The latter is disk midplane; brighter emission from the far side of the disk and fainter emission from the near side of the disk is observed as a natural consequence of a flared optically thick disk with a radial temperature gradient (decreasing temperature as a function of radius; Ohashi et al. 2022b; S. Takakuwa et al. 2023, in preparation).

The lack of a brightness asymmetry along the disk minor axis in the L1489 IRS disk could be due to its optically thin emission.In the case of the optically thin emission the entire columns are seen atboth near and far sides, resulting in a symmetric emission distribution along the minor axis. The low brightness temperature of the dustmission in the outer disk similar secondary CO snowlines have also been suggested by ($\Box 4$ K; see Figure 4) indeed suggests that the dust emission is likely optically thin except for the emission that originates from the spatially unresolved innermost region (1710)

It is also possible that the dust in the L1489 IRS disk is settled in the midplane, which causes the lack of asymmetry along the minor axis of the disk. In contrast to young Class 0/I disks, observations of Class II disks indicate that large dust grains are settled well in the midplane (e.g., Kwon et al. 2011; gas and dust emission (Panić et al. 2009; Facchini et al. 2017). Pinte et al. 2016; Villenave et al. 2020, 2022). This suggests that the dust settling occurs during the evolution from the Class I phase to the Class II phase. It has also been speculate gigure 4) is lower than that of the 180 emission (about a few that L1489 IRS is in the later evolutionary stage of the Class I dozen K; see Figure 2). This may indicate the difference in the phase based on its relatively low disk mass compared to other optical depths, although it is also possible that the dust Class I disks (Sai et al. 2020). Therefore, L1489 IRS may be inemission and the &O emission trace differentertical layers transition between the Class I and Classphases, where the dust settling has started. A similar lack of asymmetry along the minor axis is also observed in the disk around V883 Ori, which 5.5. Origin of the SO Emission: Accretion Shocks and a Warm is in transition from the Class I phase to the Class IIphase (Cieza et al.2016: Lee et al.2019).

In addition to the dust continuum emissionthe molecular line emission also shows azimuthal asymmetries (Figure 2 and shighly complex. Outside the radius of ~30 au (r \square \emptyset 2), 3). The slight shift in the emission peaks from the disk major axis to the southern side of the disk on the ¹³CO velocityintegrated emission map (Figure 3) is clear evidence 18020 emission tracesa significantly higher layer above the disk midplane (the so-called emission surface) The direction of the shift indicates that the southern side is the far side of the disk, which is consistent with the outflow configuration, in which the southern lobe is blueshifted (Yen et al. 2014). Similar molecularline structures elevated from the midplane have been observed in a number of disks (e.g., Law et al. 2021b, 2022; Lin et al. 2023). Furthermore, 1100 and C80 emissions show higher brightness temperatures on the southwestern side of the inner (r \square 0 5) disk (Figure 3). These asymmetries, as well as the nonaxisymmetric brightness distribution of the dust continuum emission, may be explained by a warped disk structure (see Section 5.6).

5.4. Gas Disk Size and Dust Disk Size

The disk size is key for undestandingdisk evolution processesSubmillimeter/millimeter observationsof Class II disks have revealed that the extent of the bright ¹²CO line emission is generally largerthan that of the dust continuum emission (e.g., Andrews et al. 2012; de Gregorio-Monsalvo et al. 2013; Ansdell et al. 2018; Long et al. 2022). This difference has been interpreted as a consequence of grain growth and radialdrift, although the difference mighalso be explained by the higher optical depth of the line emission than that of the dust continuum emission (e.g. Panić et al. 2009; Facchini et al2017; Trapman et al2019).

For the L1489 IRS disk, while the dust disk radius derived from the visibility analysis is ~230 au, the gas disk radius was estimated to be ~600 au from the rotation curve analysis of thein terms of the spatial distribution and the brightness, C¹⁸O emission (Sai et al2020). This difference of a factor of averaged ratio of gas disk radii to dust disk radii in samples of is distributed in the inner regions (□30 au) compared 100 Class II disks (Ansdell et al. 2018; Long et al. 2022), suggesting thathe dust growth and radial drift have already occurred in the L1489 IRS disk. This is also consistent with the SO emission traces a higher temperature region than is traced ring-like structure of the dustemission (see Section 5.1) and

suggests that the L1489 IRS might be in transition between the Class I phase to the Class II phase (see also Section 5.3).

However, the difference in the radii of the gas and dust disks might also be due to the difference in the optical depths of the The brightness temperature of the dust continuum emission in the outer region of the L1489 IRS disk (abouta few K; see of the disk that should have different temperatures.

Inner Disk?

As described in Section 3.2.3, the nature of the SO emission

diffuse SO emission has been observed (Figure 2). The nonuniform diffuse SO emission suggests a localized enhancement of the SO column density rather than a smooth distribution of SO within the disk. In addition, the localized enhancements of the SO brightness temperature (Figure 2) indicate the elevated gas temperaturen particular, the SO brightness temperature enhancement is prominent at r ~ 300 au on the disk major axisand this radius roughly coincides with the landing point of the accretion flow observed in the &O emission. Yen et al. (2014) reproduced the observed accretion flow with parabolic trajectories assuming a landing poin(br centrifugal radius) of ~300 au. It is thus likely that the origin of the diffuse SO emission is an accretion shock onto the protostellar disk caused by the infalling material. At the interface between the infalling material and the protostellar disk, slow shocks can occur; SO molecules are released into the gas phase due to the aerodynamic heating of dust grains in the postshock gas and/or are formed from other desorbed molecules (e.g. Aota et al. 2015; van Gelder etal. 2021). In the Class 0 protostar L1527 IR the ring-like distributions of the SO emission have been interpreted as indication of accretion shocks at the interface between the envelope and disk (Ohashi et al. 2014; Sakai et al. 2014, 2017; but see also van 't Hoff et al. 2023). SO emissions originating from the accretion shock of the late-stage infalling streamer are also observed in Class I/II disks, DG Tau and HL Tau (Garufi et al. 2022). Alternatively, the outer diffuse SO emission may originate from nonthermally desorbed SO molecules (e.g., photodesorption). However, the nonuniform distribution of the SO emission would be better explained by an accretion shock.

In the innermost region (r \square \emptyset 2), on the other hand, compact, prominent SO emission exists (Figure 3). This emission component is distinct from the outer diffuse emission suggesting a separate origin. The comparison of the radial ~2-3 in the size of the gas and dust disks is consistent with the intensity profiles (Figure 8) clearly shows that the SO emission and C18O. Given the usual temperature structure of the disk (i.e., the higher temperature at smaller radius) the compact by the CO isotopolog lines. Sai et al. (2020) calculated the temperaturestructure of the L1489 IRS disk by radiative transfer modeling. The midplane dust temperature at he SOemitting radii (□30 au) is □40 K (see Appendix C) thich is comparable to or higherthan the sublimation temperature of

²⁴ We note thatwe tried to estimate the emission surface of CO using the disksurf package (Pinte et al. 2018a; Teague et al. 2021), but no reasonable estimates were obtained due to contamination from the envelope emission.

SO (~50 K; e.g., Sakai et al. 2014; Aota et al. 2015; Miura et al. 2017), and the disk surface would be even warm the compactSO emission thus likely originates from the thermal sublimation of SO or its precursor (e.c.SHin the warm inner region. The bright emission also requires abundar 80 gas. which could be naturally explained by thermal sublimation. Although the relatively low peak brightness temperatures of SObetween the outerdisk and the innermostdisk (e.g., Nealon interpretation, the brightness temperature at the innermost region may be reduced by the beam dilution effect. Additionally, the SO emission in the innermostegion might be optically thin, resulting in a lower peak brightness temperature than the actual gas temperature.

While bright, compact SO emission is detected in the innermost region, a CH₃OH transition with an upper state energy of 45 K, which is observed in the same spectral setup. not detected. In the Class II disks around IRS 48 and HD 100546,SO emission and brightemission from complex organic molecules including CH₃OH has been detected cospatially (Booth etal. 2021a, 2021b; Brunken et al. 2022; Booth et al. 2023), indicating a hot-corino-like chemistry in the (Figure 3; see also Section 5.3). warm (□100 K) region. The detection of SO and the nondetection of CHOH in the L1489 IRS disk may indicate that the temperature is not high enough for CH₃OH ice to thermally sublimate: while the sublimation temperature of SO is ~50 K (e.g., Sakai et al. 2014; Aota et al. 2015; Miura et al. 2017), a higher temperature (~100 K) is required for GDH ice to sublimate. Alternatively, the emitting region size of CH₃OH molecules may be smallerthan that of SO, and the CH₃OH emission is thus beam diluted and/or absorbed by the bright continuum emission. Higher angular resolution observations at lower frequencies, at which the dust continuum emission is expected to be more optically thin, would be key to revealing the chemistry in the innermost region of the L1489 IRS disk.

5.6. Warped Disk Structures

We also found that the compact SO emission shows a velocity gradientalong a slightly different direction from the disk traced by ¹³CO and C¹⁸O. The left panel of Figure 9 shows the velocity-integrated intensity map of the highvelocity component(± 8-12 km s⁻¹ with respect to v_{sys}) of the redshifted and blueshifted SO emissionThe PA of the velocity gradient (\approx 82°) is slightly (\approx 15°) tilted with respect to the PA (67°) of the disk traced by ¹³CO, C¹⁸O, and dust continuum. The PV diagram of the SO emission along the PA of 82° (right panel of Figure 9) indicates that the highestvelocity component of the SO emission is fairly consistent with on a scattered-light image obtained with the Hubble Space the Keplerian velocity derived from the C18O analysis (see Section 4.2), suggesting that the compact SO emission originates from the innermost rotating disk.

The slight tilt in the velocity gradient direction is highly intriguing. While the nonaxisymmetric emission distributions in the upper layers of the disk may result in this appearance, the bust = -2 most straightforward interpretation is thathe disk is warped; the rotation axis of the innermos SO disk is slightly (≈15°) misaligned with respect to that of the outer disk, while the misalignmentmay be underestimated due to the projection effect. Observations of protostellar/protoplanetary disks have shown that many of them have misaligned or warped structures:e.g., the L1527 IRS disk (Sakaiet al. 2018) and the GW Ori disk (Bi et al. 2020; Kraus et al. 2020). In the

L1489 IRS disk, a warped structure at an outer radius of ~200 au is also found by Sai et al(2020).

With this innermost tilted disk, the observed features in both dust and molecularline emission may be explained consistently. The dust gap and the potential gas gap suggested by the C¹⁸O emission at ≈30 au (see Section 5.1) can be the boundary in the innermost region (see Figure 3) appear to contradict thiset al. 2018). Furthermore, a tilted disk can cast a shadow on the outer disk and vary the temperature of the outer disk azimuthally via irradiation (Figure 10). As a consequence, azimuthalbrightness asymmetries in the dustontinuum and molecular line emission are expected (e.g., Facchini et al. 2018; Young et al. 2021). Indeed, our observations show a slightly weaker dust continuum emission on the northeastern side of the disk (Figure 1), which is consistent with the expectation from The misalignment direction of the innermost SO disk and the configuration of the outer disk; i.e., the northeastern side is shadowed considering that e southern side is the far side of the disk (see Figure 10). The ¹³CO and C¹⁸O emissions also show lower brightness temperatures on the northeastern side

> We discuss the possible origins of the disk warp as 0 au based on our observations and theoreticatudies. Numerical simulations suggesthat warped disks can be formed by the interaction with an embedded planet (e.blealon et al.2018; Zhu 2019). If the orbital plane of the planetis inclined with respect to the outer disk, the inner disk can warp from the outer disk. If we assume that the observed gap is opened by a planet with an inclined orbit, the expected planethass from the gap depth (Section 5.1) is slightly modified. Zhu (2019) revised Equation (8) considering the inclination of the planet orbit (see also Kanagawa et al. 2015). Based on Equations (12) and (13) in Zhu (2019), the expected planethass would be a factor of ~1.4-2 higher than the estimate in Section 5.1, i.e., ~0.042–4.7 M_i, assuming orbital inclinations of 15°–90° and a typical disk aspect ratio of $h/r \sim 0.05-0.1$.

Theoreticalworks have shown that warped disk structure can also be formed by an inclined binary (e.g. Nixon et al. 2013; Facchini et al. 2018). Nixon et al. (2013) suggested that the binary torque can tear the disk and break it into two disks, an inner and an outer disk, with a misalignment. Numerical simulations of a circumbinary disk also showed that the circumbinary disk is broken into a misaligned outer and inner disk (Facchini et al. 2018). The binarity of L1489 IRS has been discussed in previous studiealthough there is stillno direct evidence that L1489 IRS is a binar ai et al. (2020) derived an upper limit on the separation of the binary (a \square 30 au) based Telescope (Padgett et al. 1999). Although our higher-resolution observations of the dust emission in millimeter wavelengths do not spatially resolve the centracompactemission either, we can provide a tighter constraint on the upper limit of the binary separation. Considering that the spatial resolution of the image is ≈0 "04 or ≈7 au and that the emission is spatially unresolved, i.e., a point source (see Appendix A), the separation would be \Box 7 au.

The question now is whether a close inclined binary like this can form the gap at~30 au that is observed in the dus(and potentially, $C^{8}O$) emission? Nixon et al. (2013) simulated the binary system with a misaligned orbit with respect to its circumbinary disk and derived a formula to estimate the diskbreaking radius. Assuming the bending-wave regime (h/r? α,

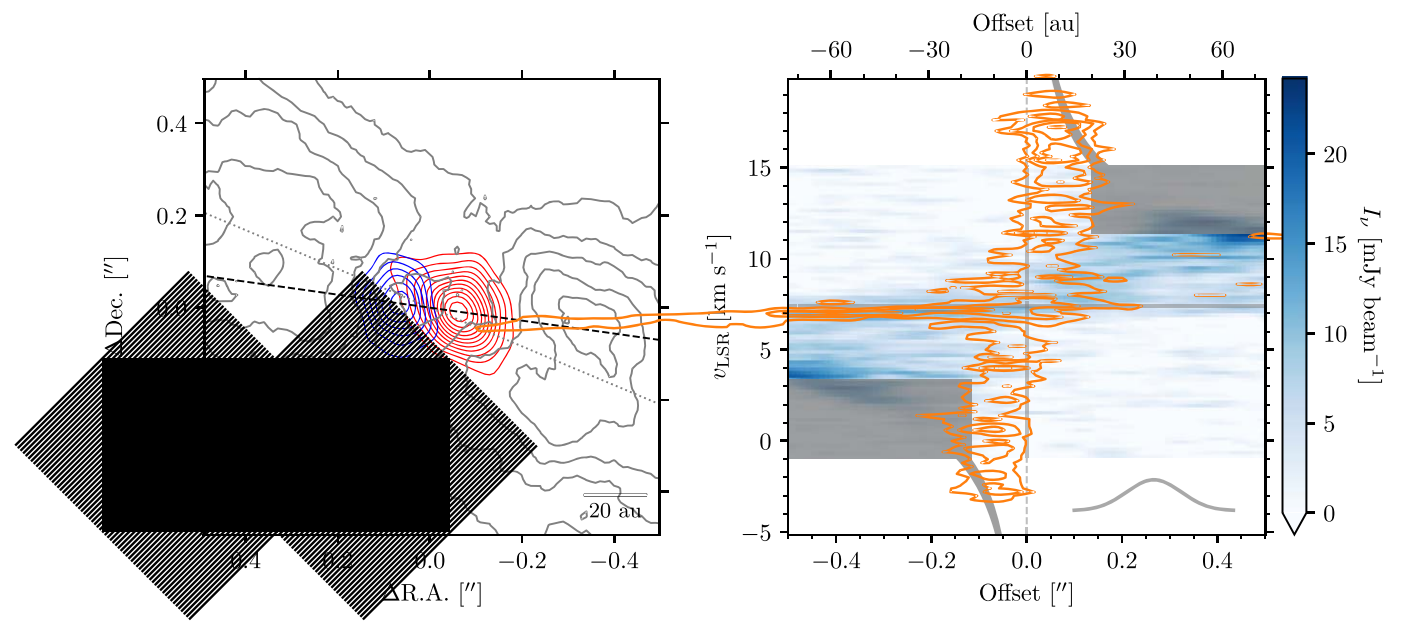


Figure 9. Left: velocity-integrated intensity map (red and blue contours for red- and blueshifted emission, respectively) of the SO emission for the highest-velocity component (± 8–12 km s̄¹ with respect to y, j), overlaid on the C̄³O velocity-integrated intensity map (gray contours; same as the middle left panel of Figure 3). The contours of the SO emission start from 5σ, followed by 2σ steps, where σ = 1.9 mJy beassī¹. The contours of the ȮO emission indicate [20, 30, 40, 50, 60, 70]σ, where σ = 1.0 mJy beassī¹ km s̄¹. While the dotted gray line marks the dust disk PA of 67estimated in the visibility analysis (see Section 4.th)e dashed black line indicates a slightly tilted PA of 82°, which approximately intercepts the peak location of the red- and blueshifted SO emission lobes. The beam is shown in the lower left corner. The scale bar in the lower right corner indicates the 20 au scale. Right: PV diagraftos entitlesion (color) along a PA of 67° and the SO emission (orange contour) along a PA of 82°. The contours indicate [3, 5, 7, 9]σ, where σ = 2.1 mJy. The shaded curves indicate the Keplerian velocity assuming the stellar mass derived from the PV diagram fits (Section 4.2). The shaded region indicates the uncertainty owing to the range of the stellar mass (1.5–1.9 M²). The Gaussian profile in the lower right corner indicates the beam size along the offset axis.

where α is the viscosity parameter), the possible maximum as disk-breaking (or gap) radius would be $\Box 2a \approx 14$ Here we assume an inclination angle of the binary orbit with respect to the disk of 45° , an equal-mass binary, and a typical disk aspect ratio of h/r ~ 0.1 , which maximizes the disk-breaking radius. While this expected maximum gap radius of ≈ 14 au does not appear to explain the observed gap radius of ~ 30 au, the latter may be overestimated due to the beam-smearing effect: the dust ring width is spatially resolved while the central compact componentis unresolved (see Table 2), and the actual gap radius (i.e., the local minima of the radial profile) could thus be smaller. Therefore, it may be possible to form the observed gap by the inner inclined binary.

Warped structuresare also formed by the change in the angular momentum in the envelope and the disk during the accretion process-lydrodynamicalsimulations show that the temporal variation of the angular momentum axis direction during the gas infall indeed results in a warped disk system (Sai et al. 2020). The outer warped structure at ~200 au observed in C¹⁸O is likely to be formed by this mechanism rather than a binary (Sai et al. 2020). Similarly, a misalignment of the magnetic field and the angular momentum axis of the core results in a warped disk (Matsumoto etal. 2017; Hirano & Machida 2019; Hirano et al. 2020). The warped structure of the L1489 IRS disk with tilts at ~30 au and ~200 au suggests a gradual change in the angular momentum axis of the infalling material.

6. Summary

We have observed the disk around the Class I protostar L1489 IRS in the 1.3 mm continuum and CO J = 2–1, $C^{18}O$ J = 2–1, and $SO_{14}J = 6_5-5_4$ lines at spatial resolutions of $^{\mu}O$ 1

as partof the eDisk ALMA Large Program.Our findings are summarized as follows:

- 1. In the 1.3 mm continuum emissionwe detected a disk-like elongated structure with nonaxisymmetric fatatils in the outermostregion (r □ 2" or ~300 au) and a ring-like structure at r ~ 04 (or ~57 au). The dust continuum ring also shows an azimuthal asymmetry, where the southwestern side is brighter than the northeastern side. We also detected a centrally peaked compaemission that is not spatially resolvedFurthermoretwo tentative shoulder-like substructureat ~1."5 (or ~220 au) and ~2.3 (or ~340 au) are also identified in the radial intensity profile of the tapered continuum image.
- 2. The high-velocity componentsof the ¹³CO and C ¹⁸O emission trace the protostelladisk. While ¹³CO originates from the disk surfaces suggested by the shift the emission peak along the disk minor axis, ⁸C traces the region near the midplane. The ¹³CO and C ¹⁸O emission also shows (slightly) higher brightnesstemperatures on the southwestern side of the disk. In the outer region (□. ¹⁶ 5), ¹³CO shows an extended structure, suggesting that traces the envelope C ¹⁸O traces the warped disk structure as well as the streamer-like accretion flow in the outer region, which is consistent with previous studies (Yen et a 2014; Sai et al. 2020).
- 3. The SO emission distribution shows a highly complex structure. While compact, prominent emission appears in the innermostregion (□♂2), the emission in the outer region is diffuse and nonuniform. The central compact componentexhibits a velocity gradient over extremely high velocities (±10–12 km s̄¹ with respect to the systemic velocity). In the outer region, multiple localized

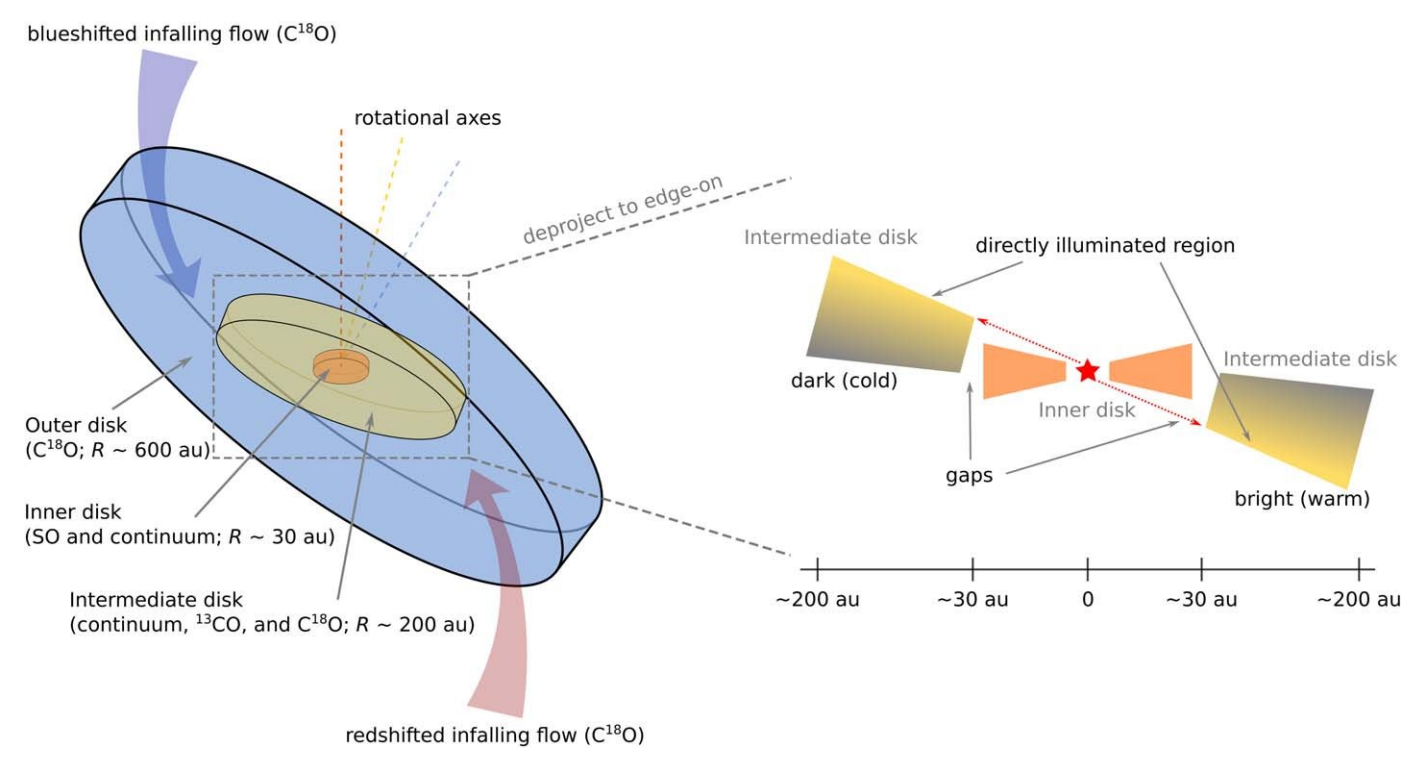


Figure 10. Schematic illustration of the L1489 IRS system. The observing configuration of the warped disk is shown in the left figure, while the right figure shows the edge-on view of the inner and intermediate disks. In the right figure, the observer is in front of the screen, but slightly on the southern side (downside), and thus the brightness asymmetry (i.ethe western side is brighter than the eastern side) is observed.

enhancements of the peak brightness temperature are identified.

- 4. We performed an analytical fit to the dust continuum emission in the visibility domain, from which we confirm that the observed visibility can be explained by a simple model that consists of two Gaussian components(a central compact and an outer extended component) and one Gaussian ring at r = 0.739 (or 56 au). We also precisely characterized the properties of each component and the dust disk geometry through the fit. While the centralcomponents guite compact(~1 au), the size of the outer component is ~540 au. The disk inclination and PAs are also constrained to be 72° and 67°, respectively.
- 5. We estimated the central stellar mass through an analysis of the C18O PV diagram. The estimated centrastellar mass of 1.5-1.9 Me is consistent with previous studies (Yen et al. 2014; Sai et al. 2020).
- 6. We discuss the possible origin of the observed substructures. The coincidence between the dust ring and the peak of the C⁸O radial intensity profile suggests that the gas disk also has a ring/gap structure. If we assume that the gas gap is carved by a formed planet, the planet mass would be ~0.6 M_{Jup} Alternatively, grain growth may be responsible for the observed dusting because the ring radius is consistent with the prediction of the dust coagulation model.
- 7. The nonuniform distributions and localized brightness origin of the outer diffuse SO emission is likely to be an accretion shock caused by the infalling materian the other hand, we suggest that the central compact componentoriginates from the thermal sublimation of

- Indeed, the disk model of L1489 IRS shows a midplane dust temperature of \(\subseteq 40 \) K at the SO-emitting radii, which is comparable to the sublimation temperature of SO (~50 K).
- 8. We also find that the velocity structure of the compact SO emission is consistent with Keplerian rotation and that its velocity gradientdirection is slightly (≈15°) misaligned with respect to that of the disk traced bcO and C8O. We propose that the inner disk is tilted e., the rotation axis of the inner disk traced by SO is misaligned with respect to the outer disk traced by 3CO and C18O. The disk misalignment cause a shadowed region in the outer disk, which explains the observed azimuthal asymmetry in the brightness of the dust and molecular line emission. We discuss the possible origins of the misalignment, a planet or a binary with an inclined orbit, or a temporal variation in the angular momentum axis direction during the gas infall.
- 9. Combined with previous studiesthe L1489 disk has a warped structure with tilts at ~30 au and ~200 au (Figure 10). While the tilt at ~30 au can be explained by a planet or a binary with an inclined orbit, a temporal variation in the angular momentum axis direction during the gas infall might explain the whole warped structure.

Acknowledgments

temperature increases in the SO emission suggest that the This paper makes use of the following ALMA data: ADS/JAO. ALMA#2019.1.00261.L, ADS/JAO.ALMA#2019.A.00034.S.

ALMA is a partnership of ESO (representing its member states),NSF (USA) and NINS (Japan), together with NRC (Canada) MOST and ASIAA (Taiwan), and KASI (Republic SO and/or its precursor molecules at the warm inner disk.of Korea), in cooperation with the Republic of Chile. The Joint ALMA Observatory is operated by ESO, AUI/NRAO and NAOJ. The National Radio Astronomy Observatory is a facility of the National Science Foundation operated under cooperative agreement by Associated Universities, Inc. Y.Y. is Jefferson ScholarsFoundation, the NRAO ALMA Student supported by the International Graduate Program for Excellence in Earth-Space Science (IGPEES), World-leading Innovative Graduate Study (WINGS) Program of the University of Tokyo. Y.A. acknowledgessupport by NAOJ ALMA Scientific Research Grant code 2019-13B, Grant-in-Aid for Scientific Research (S)18H05222, and Grant-in-Aid for Transformative Research Areas (A) 20H05844 and 20H05847. N.O. acknowledges support from National Science through the GraduateResearch Fellowship Program under NSTC 109-2112-M-001-051 and 110-2112-M-001-03/IJ.T. acknowledgessupport from NASA XRP 80NSSC22K1159. J.K.J. and R.S. acknowledge supporfrom the Independent Research Fund Denmark (grantNo. 0135-00123B).S.T. is supported by JSPS KAKENHI grant No. 21H00048 and 21H04495. This work was supported by NAOJ ALMA Scientific Research GrantCode 2022-20A. I.d.G. acknowledges support from grant PID2020-114461GB-100nded by MCIN/AEI/10.13039/501100011033. P.M.K. acknowledges supportfrom NSTC 108-2112- M-001-012NSTC 109-2112-M-001-022 and NSTC 110-2112-M-001-057. W.K. was supported by the National Research Foundation of Korea (NRF) grant funded by the Korea government (MSIT; NRF-2021R1F1A1061794)S.P.L. and T.J.T. acknowledge grants from the National Science and Technology Council of Taiwan 106-2119-M-007-021-MY3and 109-2112-M-007-010-MY3. C.W.L. is supported by the Basic Science Research Program through the National Research Foundation ofKorea (NRF) funded by the Ministry of Education, Science and Technology (NRF- 2019R1A2C1010851) and by the Korea Astronomy and Space Science Institute grant funded by the Korea government(MSIT; Project No. 2022-1-840-05).J.E.L. is supported by the National Research Foundation of Korea (NRF) grantfunded by the Korean governmen(MSIT; grant

number 2021R1A2C1011718\(\bar{L}\). Y.L. is supported in partby NASA NSSC20K0533 and NSF AST-1910106, Z.Y.D.L. acknowledgessupport from NASA 80NSSC18K1095, the Observing Support (SOS) SOSPA8-003, the Achievements Rewards for College Scientists (ARC\$pundation Washington Chapter, the Virginia Space Grant Consortium (VSGC), and UVA research computing (RIVANNA)L.W.L. acknowledges supported by JSPS KAKENHI grantNo. JP21J00086 and 22K1408 S.N. acknowledges support the National Science Foundation and Technology Council (NSTC) in Taiwan through the grants Grant No. 2236415. Any opinions, findings, and conclusions or recommendations expressed in this materizate those of the authors and do not necessarily reflect the views of the National Science Foundation. V.Y. acknowledges suppoftom the National Science and Technology Coun(INSTC) in Taiwan through the grant NSTC 110-2628-M-001-003-MY3 and from the Academia Sinica CareeDevelopmentAward (AS-CDA-111-M03). M.L.R.H. acknowledges support from the Michigan Society of Fellows.

Facility: ALMA.

Software: astropy (Astropy Collaboration et al. 2013), (Teague & Foreman-Mackey 2018), bettermoments GALARIO (Tazzari et al. 2018), emcee (Foreman-Mackey et al. 2013), SLAM (Aso & Sai 2023), disksurf (Teague et al. 2021).

Appendix A Continuum Maps with Different Robust Parameters

Figure A1 shows the continuum emission maps in the central region imaged with different robust parameters, anging from -2.0 (similar to uniform weighting) to 2.0 (similar to natural weighting). The central compact component is not spatially resolved even with robust = - 2.0, where the beam size is 0.041×0.023 (or 6.9 × 3.4 au).

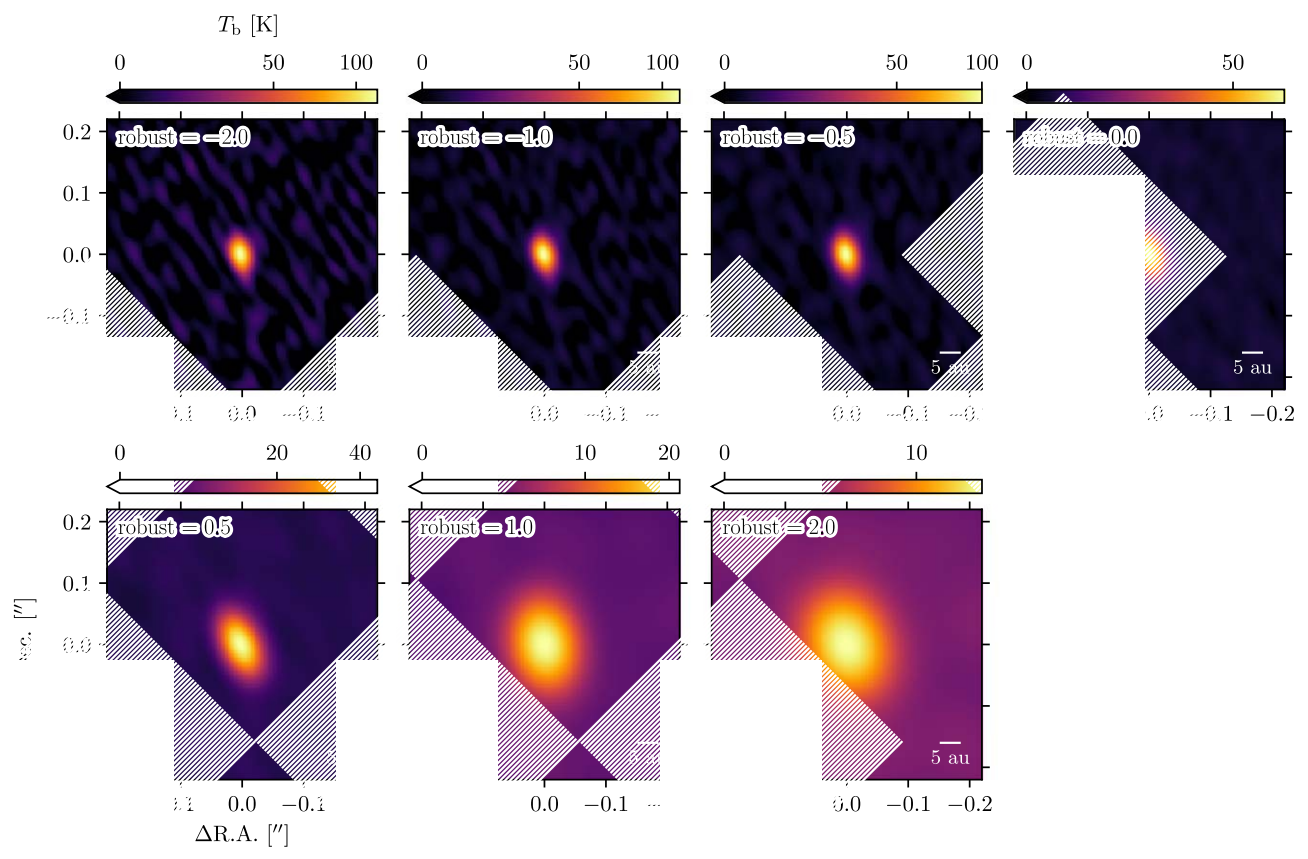
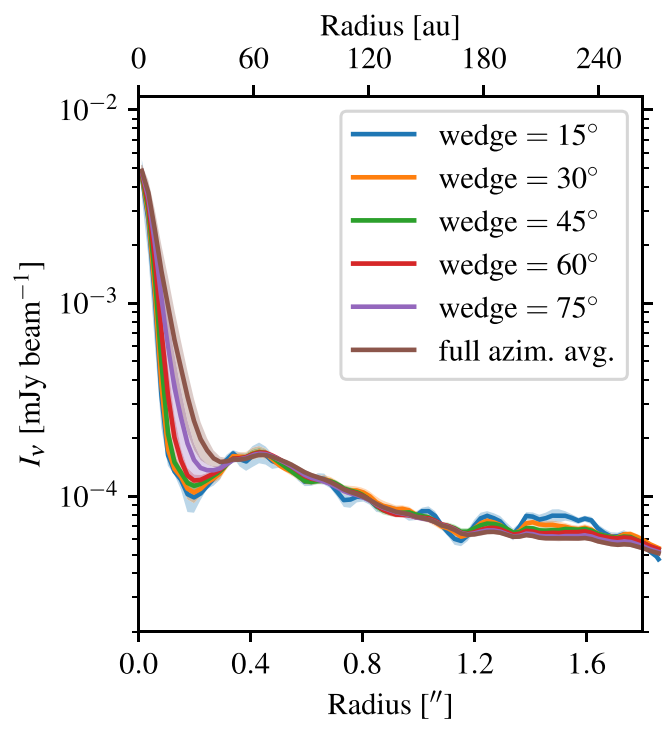


Figure A1. Continuum emission in the central region imaged with different robust parameters (-2.0, -1.0, -0.5, 0.0, 0.5, 1.0, and 2.0). In each panel, the beam size and 5 au scale are indicated in the lower left and right cornespectively.

Appendix B Generation and Selection of Radial Intensity Profiles

and selecting the radial intensity profiles of the continuum and compare them in Figure B1While the wider wedges resulted line emission. We follow the method described in Law etal. To deproject the disk coordinates we assume a disk geometry (i = 72° and PA =67°) that is based on the results of the visibility analysis (Section 4.1) for both continuum and line profiles. The radial bin size is one-quarter of the major axis of bin. The uncertainty is calculated as the standard error in the region over which the emission is average the generated the

continuum intensity profiles averagedover several certain azimuthalwedges (±15°, ± 30°, ± 45° and ±90°; i.e., full In this section, we describe the detailed method for generating imuthal average) with respect to the disk major axis, and low-contrastsubstructures due to the coarseffective resolu-(2021a). We generate the profiles by deprojecting the emission tions in the inclined disk, narrower wedges show wavy features maps (continuum) or velocity-integrated emission maps (line), that are not considered actual substructures in the outer radii. We selected the profile with a ±45° wedge as the representative profiles to compromise between these two effects: the line emission, we choose the same wedge (±45°) as for the continuum emission to generate the radiatensity profiles at the synthesized beam. We averaged the emission in each radisimilar effective resolutions. We note that the deprojection here assumes a geometrically thin disk and does not consider the 3D structures of the disk.



differentazimuthalwedges (averaged overth sides of the disk). Each color represents the radial profile extracted from ±15°, ±30°, ±45°, ±60°, ±75°, and ±90° (i.e., full azimuthal average) wedges with respect to the major axis of the Nguyen Thi Phuong® https://orcid.org/0000-0002disk. The color-shaded regions represent the uncertainty of the profiles.

Appendix C Radiative Transfer Model of the L1489 IRS Disk

Figure C1 shows the dust temperature profiles of the L1489 IRS disk at different disk scale heights (h/r = 0.0, midplane; 0.15, and 0.3) calculated bwith the radiative transfer Merel L. R. van 't Hoff https://orcid.org/0000-0002modeling by Sai et al. (2020). We refer to the original paper for 2555-9869 details of the modeling. In the emitting region of SO (the inset Hsi-Wei Yen https://orcid.org/0000-0003-1412-893X of Figure C1), the dust temperature ishigher than ~40 K, comparable to the sublimation temperature &O molecules (~50 K; see Section 5.5).

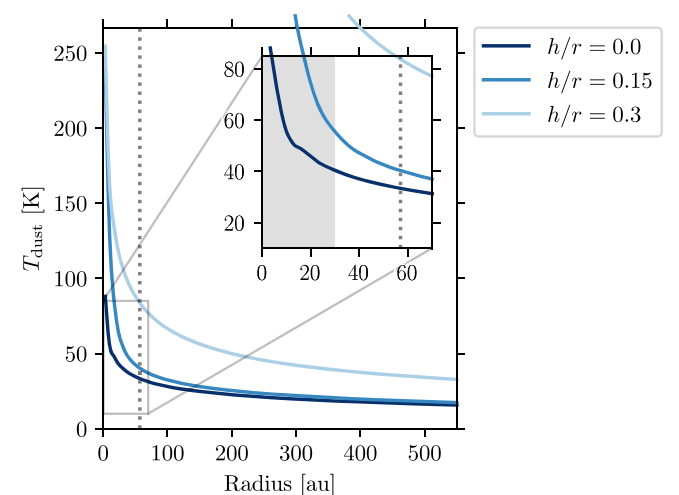


Figure C1. Dust temperature profiles of the L1489 IRS disk at selected scale heights (h/r = 0.0, midplane; 0.15, and 0.3), based on the radiative transfer calculation by Sai et al. (2020). The inset axis shows the inner region for visual clarity. The vertical dotted lines in the main and inset axes indicate the locationBrinch, C., Crapsi, A., Jørgensen, K., Hogerheijde, M. R., & Hill, T. 2007, of the dust ring. The gray shaded region in the inset axis is the approximate SOemitting region.

ORCID iDs

Yoshihide Yamato https://orcid.org/0000-0003-4099-6941 Yuri Aikawa https://orcid.org/0000-0003-3283-6884 Nagayoshi Ohashi https://orcid.org/0000-0003-0998-5064 John J.Tobin https://orcid.org/0000-0002-6195-0152 Jes K.Jørgensen https://orcid.org/0000-0001-9133-8047 Shigehisa Takakuwa https://orcid.org/0000-0003-0845-128X

Yusuke Ason https://orcid.org/0000-0002-8238-7709 Jinshi Sai (Insa Choi) https://orcid.org/0000-0003-4361-5577

Christian Flores https://orcid.org/0000-0002-8591-472X Itziar de Gregorio-Monsalvo https://orcid.org/0000-0003-4518-407X

Shingo Hirano https://orcid.org/0000-0002-4317-767X Ilseung Han https://orcid.org/0000-0002-9143-1433 Mivu Kido https://orcid.org/0000-0002-2902-4239 Patrick M. Koch https://orcid.org/0000-0003-2777-5861 Woojin Kwon https://orcid.org/0000-0003-4022-4132 Shih-Ping Lai® https://orcid.org/0000-0001-5522-486X Chang Won Lee https://orcid.org/0000-0002-3179-6334 Jeong-Eun Lee https://orcid.org/0000-0003-3119-2087 Zhi-Yun Li https://orcid.org/0000-0002-7402-6487 Zhe-Yu Daniel Lin https://orcid.org/0000-0001-7233-4171 Figure B1. Comparison of the radial continuum intensity profiles generated with eslie W. Looney https://orcid.org/0000-0002-4540-6587 Shoji Mori https://orcid.org/0000-0002-7002-939X Suchitra Narayanan https://orcid.org/0000-0002-0244-6650

> Alejandro Santamaría-Miranda https://orcid.org/0000-0001-6267-2820

Rajeeb Sharma https://orcid.org/0000-0002-0549-544X Travis J. Thieme[®] https://orcid.org/0000-0003-0334-1583 Kengo Tomida https://orcid.org/0000-0001-8105-8113

References

ALMA Partnership, Brogan, C. L., Pérez, L. M., et al. 2015, ApJL, 808, L3 Alves, F. O., Girart, J. M., Caselli, P., et al. 2017, A&A, 603, L3 Andrews, S. M., Huang, J., Pérez, L. M., et al. 2018, ApJL, 869, L41 Andrews, S. M., & Williams, J. P. 2005, ApJ, 631, 1134 Andrews, S. M., Wilner, D. J., Hughes, A. M., et al. 2012, ApJ, 744, 162 Ansdell, M., Williams, J. P., Trapman, L., et al. 2018, ApJ, 859, 21 Ansdell, M., Williams, J. P., van der Marel, N., et al. 2016, ApJ, 828, 46 Aota, T., Inoue, T., & Aikawa, Y. 2015, ApJ, 799, 141 Aso, Y., & Machida, M. N. 2020, ApJ, 905, 174 Aso, Y., Ohashi, N., Saigo, K., et al. 2015, ApJ, 812, 27 Aso, Y., & Sai, J. 2023, jinshisai/SLAM: First Release of SLAM, v1.0.0, Zenodo,doi:10.5281/zenodo.7783868 Astropy Collaboration, Robitaille, T. P., Tollerud, E. J., et al. 2013, A&A, 558, A33 Bae, J., Teague, R., Andrews, S. M., et al. 2022, ApJL, 934, L20 Beckwith, S. V. W., Sargent, A. I., Chini, R. S., & Guesten, R. 1990, AJ, Benisty, M., Bae, J., Facchini, S., et al. 2021, ApJL, 916, L2 Bi, J., van der Marel, N., Dong, R., et al. 2020, ApJL, 895, L18 Booth, A. S., Ilee, J. D., Walsh, C., et al. 2023, A&A, 669, A53 Booth, A. S., van der Marel, N., Leemker, M., van Dishoeck, E. F., & Ohashi, S. 2021a, A&A, 651, L6

Booth, A. S., Walsh, C., Terwisscha van Scheltingal,, et al. 2021b, NatAs,

Brunken, N. G. C., Booth, A. S., Leemker, M., et al. 2022, A&A, 659, A29

```
Casassus, & Cárcamo, M. 2022, MNRAS, 513, 5790
Cataldi, G., Yamato, Y., Aikawa, Y., et al. 2021, ApJS, 257, 10
Cieza,L. A., Casassus,, Tobin, J., et al. 2016, Natur, 535, 258
Czekala,I., Loomis, R. A., Teague, R., et al. 2021, ApJS, 257, 2
de Gregorio-Monsalvo, I., Ménard, F., Dent, W., et al. 2013, A&A, 557, A133
Dutrey, A., Guilloteau, S., Piétu, V., et al. 2017, A&A, 607, A130
Endres, C. P., Schlemmer, S., Schilke, P., Stutzki, J., & Müller, H. S. P. 2016,
       Sp. 327. 95
Facchini, S., Birnstiel, T., Bruderer, S., & van Dishoeck, E. F. 2017, A&A,
  605, A16
Facchini, S., Juhász A., & Lodato, G. 2018, MNRAS, 473, 4459
Flores, C., Duchêne, G., Wolff, S., et al. 2021, AJ, 161, 239
Foreman-MackeyD., Hogg, D. W., Lang, D., & Goodman, J. 2013, PASP,
   125,306
Garufi, A., Podio, L., Codella, C., et al. 2022, A&A, 658, A104
Harsono, D., Bjerkeli, P., van der Wiel, M. H. D., et al. 2018, NatAs, 2, 646
Hirano, S., & Machida, M. N. 2019, MNRAS, 485, 4667
Hirano, S., Tsukamoto, Y., Basu, S., & Machida, M. N. 2020, ApJ, 898, 118
Hogerheijde, M. R., & Sandell, G. 2000, ApJ, 534, 880
Hogerheijde, M. R., van Dishoeck, E. F., Blake, G. A., & van Langevelde, H. J.
   1998, ApJ, 502, 315
Jorsater, S., & van Moorsel, G. A. 1995, AJ, 110, 2037
Kanagawa, K. D., Muto, T., Tanaka, H., et al. 2015, ApJL, 806, L15
Keppler, M., Benisty, M., Müller, A., et al. 2018, A&A, 617, A44
Kraus, S., Kreplin, A., Young, A. K., et al. 2020, Sci, 369, 1233
Kwon, W., Looney, L. W., & Mundy, L. G. 2011, ApJ, 741, 3
Lambrechts M., & Johansen A. 2014, A&A, 572, A107
Law, C. J., Crystian, S., Teague, R., et al. 2022, ApJ, 932, 114
Law, C. J., Loomis, R. A., Teague, R., et al. 2021a, ApJS, 257, 3
Law, C. J., Teague, R., Loomis, R. A., et al. 2021b, ApJS, 257, 4
Lee, C.-F., Li, Z.-Y., Ho, P. T. P., et al. 2017, SciA, 3, e1602935
Lee, C. W., Kim, G., Myers, P. C., et al. 2018, ApJ, 865, 131
Lee, J.-E., Lee, S., Baek, G., et al. 2019, NatAs, 3, 314
Lin, Z.-Y. D., Li, Z.-Y., & Tobin, J. J. 2023, ApJ, 951, 9
Long, F., Andrews, S. M., Rosotti, G., et al. 2022, ApJ, 931, 6
Maret, S., Maury, A. J., Belloche, A., et al. 2020, A&A, 635, A15
Matsumoto, T., Machida, M. N., & Inutsuka, S.-i. 2017, ApJ, 839, 69
McMullin, J. P., Waters, B., Schiebel, D., Young, W., & Golap, K. 2007, in
   ASP Conf. Ser. 376, Astronomical Data Analysis Software and Systems
   XVI, ed. R. A. Shaw, F. Hill, & D. J. Bell (San Francisco, CA: ASP), 127
Mercimek, S., Codella, C., Podio, L., et al. 2022, A&A, 659, A67
Miura, H., Yamamoto, T., Nomura, H., et al. 2017, ApJ, 839, 47
Motte, F., & André, P. 2001, A&A, 365, 440
Müller, H. S. P., Schlöder, F., Stutzki, J., & Winnewisser, G. 2005, JMoSt,
   742,215
Müller, H. S. P., Thorwirth, S., Roth, D. A., & Winnewisser, G. 2001, A&A,
   370.L49
Nealon, R., Dipierro, G., Alexander, R., Martin, R. G., & Nixon, C. 2018,
   MNRAS, 481, 20
Nixon, C., King, A., & Price, D. 2013, MNRAS, 434, 1946
Öberg, K. I., Furuya, K., Loomis, R., et al. 2015, ApJ, 810, 112
Öberg, K. I., Guzmán, V. V., Walsh, C., et al. 2021, ApJS, 257, 1
Ohashi, N., Saigo, K., Aso, Y., et al. 2014, ApJ, 796, 131
Ohashi, N., Tobin, J. J., Jorgensen J. K., et al. 2023, ApJ, 951, 8
Ohashi, S., Kobayashi, H., Nakatani, R., et al. 2021, ApJ, 907, 80
```

```
Ohashi, S., Kobayashi, H., Sai, J., & Sakai, N. 2022a, ApJ, 933, 23
Ohashi, S., Nakatani, R., Liu, H. B., et al. 2022b, ApJ, 934, 163
Okuzumi, S., Momose, M., Sirono, S.-i., Kobayashi, H., & Tanaka, H. 2016,
Padgett, D. L., Brandner, W., Stapelfeldt, K. R., et al. 1999, AJ, 117, 1490
Panić, O., Hogerheijde, M. R., Wilner, D., & Qi, C. 2009, A&A, 501, 269
Pinte, C., Dent, W. R. F., Ménard, F., et al. 2016, ApJ, 816, 25
Pinte, C., Ménard, F., Duchêne, G., et al. 2018a, A&A, 609, A47
Pinte, C., Price, D. J., Ménard, F., et al. 2018b, ApJL, 860, L13
Roccatagliata, V., Franciosini, E., Sacco, G. G., Randich, S., &
   Sicilia-Aguilar, A. 2020, A&A, 638, A85
Ruíz-Rodríguez, D., Cieza, L. A., Williams, J. P., et al. 2017, MNRAS,
   468, 3266
Sai, J., Ohashi, N., Maury, A. J., et al. 2022, ApJ, 925, 12
Sai, J., Ohashi, N., Saigo, K., et al. 2020, ApJ, 893, 51
Sakai, N., Hanawa, T., Zhang, Y., et al. 2018, Natur, 565, 206
Sakai, N., Oya, Y., Higuchi, A. E., et al. 2017, MNRAS Lett., 467, L76 Sakai, N., Sakai, T., Hirota, T., et al. 2014, Natur, 507, 78
Segura-Cox, D. M., Schmiedeke, A., Pineda, J. E., et al. 2020, Natur,
   586, 228
Seifried, D., Sánchez-MongeÁ, Walch, S., & Banerjee, R. 2016, MNRAS,
SheehanP. D., & Eisner, J. A. 2017, ApJ, 851, 45
SheehanP. D., & Eisner, J. A. 2018, ApJ, 857, 18
SheehanP. D., Tobin, J. J., FedermanS., Megeath, S. T., & Looney, L. W.
   2020, ApJ, 902, 141
Takahashi S. Z., & Muto, T. 2018, ApJ, 865, 102
Tamura, M., Gatley, I., Waller, W., & Werner, M. W. 1991, ApJL, 374, L25
Tazzari, M., Beaujean F., & Testi, L. 2018, MNRAS, 476, 4527
Teague R., Bae, J., & Bergin, E. A. 2019, Natur, 574, 378
Teague, R., & Foreman-Mackey, D. 2018, RNAAS, 2, 173
Teague, R., Law, C. J., Huang, J., & Meng, F. 2021, JOSS, 6, 3827
Tobin, J. J., SheehanP. D., Megeath,S. T., et al. 2020, ApJ, 890, 130
Trapman, L., Facchini, S., Hogerheijde, M. R., van Dishoeck, E. F., &
   Bruderer, S. 2019, A&A, 629, A79
Tychoniec,Ł., van Dishoeck,E. F., van 't Hoff, M. L. R., et al. 2021, A&A,
   655, A65
van der Marel, N., van Dishoeck, E. F., Bruderer, S., et al. 2013, Sci, 340,
van Gelder, M. L., Tabone, B., van Dishoeck, E. F., & Godard, B. 2021, A&A,
van 't Hoff, M. L. R., Harsono, D., Tobin, J. J., et al. 2020, ApJ, 901, 166
van 't Hoff, M. L. R., Tobin, J. J., Li, Z.-L., et al. 2023, ApJ, 951, 10
Villenave, M., Ménard, F., Dent, W. R. F., et al. 2020, A&A, 642, A164
Villenave, M., Stapelfeldt, K. R., Duchêne, G., et al. 2022, ApJ, 930, 11
Weaver, E., Isella, A., & Boehler, Y. 2018, ApJ, 853, 113
Yen, H.-W., Takakuwa, S., Ohashi, N., et al. 2014, ApJ, 793, 1
Yen, H.-W., Takakuwa, S., Ohashi, N., & Ho, P. T. P. 2013, ApJ, 772, 22
Young, A. K., Alexander, R., Walsh, C., et al. 2021, MNRAS, 505, 4821
Zhang, K., Blake, G. A., & Bergin, E. A. 2015, ApJL, 806, L7
Zhang, K., Booth, A. S., Law, C. J., et al. 2021, ApJS, 257, 5
Zhang, S., Zhu, Z., Huang, J., et al. 2018, ApJL, 869, L47
Zhu, Z. 2019, MNRAS, 483, 4221
Zucker, C., Speagle, J. S., Schlafly, E. F., et al. 2019, ApJ, 879, 125
Zucker, C., Speagle J. S., Schlafly, E. F., et al. 2020, A&A, 633, A51
```